Journal of Computational Physics 229 (2010) 2401–2421

Contents lists available at ScienceDirect

Journal of Computational Physics

journal homepage: www.elsevier.com/locate/jcp

Simulation of concentrated suspensions using the force-coupling method

Kyongmin Yeo, Martin R. Maxey *

Division of Applied Mathematics, Brown University, Providence, RI 02912, USA

ARTICLE INFO

Article history:
Received 19 May 2009
Accepted 25 November 2009
Available online 4 January 2010

Keywords:
Force-coupling method
Lubrication correction
Suspension flows
Stokes flow

ABSTRACT

The force-coupling method (FCM) represents the dynamics of low Reynolds number suspension flows through a distributed, low-order, finite force-multipole expansion and provides an efficient, matrix-free method to solve the mobility problem for the particle motion. In concentrated suspensions, strong short-range lubrication forces are generated between particles in close proximity as fluid in the intervening gap is displaced by the relative motion of the particles. These forces, together with near-surface contact forces, play an important role in the suspension rheology and self-diffusion of particles. However these forces lead to ill-conditioned problems for determining the particle stresses and particle motion in large systems of particles at higher volume fractions. A robust and effective iteration scheme for determining the particle stresslets is described together with a new scheme for including lubrication forces as near-field corrections to the FCM resistance problem. Both the lubrication and far-field interactions are solved as fully coupled systems in $O(N_p \log(N_p))$ operations, for N_p particles, using preconditioned conjugate gradient solvers. Numerical results for particles settling under gravity, particle pairs in linearly varying flows and in concentrated suspensions are compared with previous theoretical results and simulations. Numerical simulations with more than 4000 non-Brownian, spherical particles in a homogeneous shear flow provide results on the pair-distribution function and Lagrangian velocity correlations. The extension of the methods to simulate bidisperse systems or wall-bounded suspensions are discussed.

1. Introduction

Suspensions of small particles in low Reynolds number flows have been the subject of detailed study for several decades. They are relevant to a wide range of engineering and biological applications; materials processing, particle coating, microdevices for particle separation or mixing, waste treatment, blood flow and cell adhesion, to name a few. Concentrated suspensions are characterized by both the long-range multi-body hydrodynamic interactions of particles and the short-range viscous lubrication forces that act between particles near to contact. For example, the volume fraction of red blood cell in human blood flow is typically ~45% [1]. Even in nominally dilute suspensions, both long-range flow interactions and short-range lubrication forces are important for particles in microfluidic devices where particles are confined by flow geometry [2,3].

Numerical simulations of monodisperse suspension flows in uniform shear have had a large impact on the characterization and modeling of low Reynolds number suspensions. The principal tools have been Stokesian Dy-namics (SD) [4], multipole expansions [5–7], and boundary integral methods [8]. Lattice-Boltzmann methods (LBM) bridge both finite Reynolds number and low Reynolds number systems and have also contributed [9,10]. The force-coupling method (FCM) [11,12] and subsequent

* Corresponding author. Tel.: +1 401 863 1482; fax: +1 401 863 2722.
E-mail address: maxey@dam.brown.edu (M.R. Maxey).

0021-9991/$ - see front matter © 2009 Elsevier Inc. All rights reserved.
doi:10.1016/j.jcp.2009.11.041

developments, bridge both Stokes flows and finite, low Reynolds number systems. FCM may be used to simulate large systems of particles in both open and wall-bounded flows in fully three-dimensional configurations.

For the accurate simulation of Stokes flow, a numerical method should be able to capture both the long-range multi-body interactions and the short-range lubrication interactions. Especially, the singular nature of the lubrication forces hinders the development of numerical schemes. For example, the most straightforward and exact numerical method would be the direct numerical simulation with an arbitrary Lagrangian–Eulerian technique [13,14]. However, considering that the lubrication forces for the normal and tangential motions between a particle pair are, respectively, $\sim 1/\epsilon$ and $\log\epsilon$, in which $a\epsilon$ denotes the separation distance between two particles and a is the particle radius, the grid spacing should be smaller than at least $10^{-3}a$—$10^{-4}a$ to resolve the lubrication forces. Correspondingly, the time step size also should be very small, of the order of 10^{-3}—10^{-4}, making long-term simulations of the suspension dynamics too costly.

In Stokes flow, the hydrodynamic interactions are determined solely by the instantaneous configuration of particles. Using the special properties of Stokes flow, several numerical methods have been developed focusing on computing hydrodynamic interactions rather than resolving the whole flow field. The multipole expansion is a representative approach to consider the hydrodynamic interactions between particles. However, Cichocki and Felderhof [5] reported that the number of multipole moments needed to resolve the hydrodynamic interaction becomes impractically large as the gap between particles becomes so small that the lubrication force plays an important role. Durlofsky et al. [15] developed the Stokesian Dynamics method, which is a low-order multipole representation, supplemented by short-range lubrication forces, to compute the position and movement of suspended particles. In the Stokesian Dynamics, they assumed the lubrication interaction can be added in a pair-wise manner in the resistance formulation, which has become a standard approach for incorporating the lubrication forces [6,9,16]. Sierou and Brady [17] developed the Accelerated Stokesian Dynamics (ASD) method and performed the simulations of up to 1000 particles [18].

The boundary element method (BEM) is another distinguishing numerical method for Stokes flows, see for example [8]. BEM can calculate the hydrodynamic interactions in particulate suspensions with greater accuracy. However, even here some form of lubrication or contact forces must be included between rigid particles. Ingber et al. [19] have developed a traction-corrected BEM which can accurately calculate the lubrication interaction. Although BEM can simulate wall-bounded suspensions and suspension of particles with arbitrary shapes [20,21], due to the high computational cost most simulations are done in 2-dimensions or with relatively small numbers of particles.

Since Nguyen and Ladd [9] implemented the lubrication interaction into the lattice-Boltzmann simulation, LBM has become popular for the suspensions in the low to finite Reynolds number flows [10,22,23]. Compared to SD, LBM is computationally inexpensive and a rigid wall boundary can be included without any special treatment, while present techniques for SD use an image method [24,25] or wall particles [26,27] to represent a rigid wall.

Maxey and Patel [11] developed the force-coupling method (FCM) for Stokes flow by replacing the Dirac delta function in the standard multipole expansion [28] by a localized force envelope. The force-coupling method has been verified [29,12,30] and applied in many suspension flows; for example, a sedimentation problem [31], bimodal suspensions [32], turbulent flows [33], and biological flows [34]. Since multi-body hydrodynamic interactions are accounted for by solving the Stokes equation, the computational cost of FCM depends on the choice of the Stokes solver. In a periodic domain, the long-range hydrodynamic interactions can be calculated in $O(N_p log N_p)$ operations using a Fourier spectral method, in which N_p is the number of particles. Dance and Maxey [31] performed the numerical simulations of particle sedimentation with up to 10,000 particles. The force-coupling method can be implemented with any existing flow solver by adding functions to integrate and project the force envelope. Recently, Liu et al. [35] showed that the force-coupling method can simulate suspensions of ellipsoidal particles by appropriately rescaling the force envelopes.

In the force-coupling method, the translational and angular velocities of a particle are estimated by the local average of the fluid velocity weighted by the corresponding force envelopes. This approach has a computational advantage by reducing the number of grid points necessary to resolve a particle. Once the resolution is fine enough to resolve the force envelope, FCM can accurately reproduce the far-field solution. Typically, it requires only $a/\Delta x \simeq 3$ to resolve a particle in which Δx is the grid spacing. This is less than other methods, such as the immersed boundary method or the lattice-Boltzmann simulations. On the other hand, it has a disadvantage that the near-field solution is not correctly resolved. When two particles are close, the force-coupling method cannot reproduce the lubrication effects [12]. As a result, the force-coupling method has been used mainly for low volume fractions, $\phi < 0.1$.

Dance and Maxey [36] developed a method to incorporate the lubrication effects into the force-coupling method based on the exact solution of the viscous lubrication interactions of a particle–pair. They employed a predictor–corrector type approach. First, the far-field interaction is calculated by the standard FCM to estimate the lubrication force and then the lubrication force is used as a feedback force in the mobility formulation. By construction, their method can reproduce the exact particle velocities for a particle–pair interaction. At low volume fractions in which most lubrication interactions are from particle doublets, the 'lubrication barrier' would be sufficient [32]. However, it is not straightforward how to generalize the approach to include multi-body interactions, which generally requires the addition of lubrication interactions to a resistance formulation [15].

The main goal of this paper is to develop an efficient method to incorporate the lubrication forces for general volume fractions into the force-coupling method. The lubrication correction method developed in this paper can be easily extended to the bidisperse suspensions or the wall-bounded flows [37].

In Section 2, the brief introduction and the discretized equation of the force-coupling method are given and it is shown that the force-coupling method in Stokes flow can be expressed in terms of a mobility problem. A new efficient and robust iterative scheme to calculate the stresslet is introduced. The lubrication correction method for the force-coupling method is developed by applying the pair-wise additivity approximation in Section 3. In Section 4, the numerical simulations of the spheres in the infinite domain are performed to verify the present lubrication correction method. Section 5 illustrates the numerical simulations of the concentrated suspensions. Finally, the conclusions are given in Section 6.

2. Force-coupling method

2.1. Review of the force-coupling method

The equations of the fluid motion with the force-coupling method are

$$\nabla p(\boldsymbol{x}) = \mu\nabla^2\boldsymbol{u}(\boldsymbol{x}) + \boldsymbol{f}(\boldsymbol{x}), \tag{1}$$

$$\nabla\cdot\boldsymbol{u} = 0, \tag{2}$$

in which p is pressure, μ is viscosity of the fluid, $\boldsymbol{u}$ is fluid velocity. The force density $\boldsymbol{f}$ is defined as

$$f_i(\boldsymbol{x}) = \sum_{n=1}^{N_p}\left\{F_i^n\Delta_M(\boldsymbol{x}-\boldsymbol{Y}^n) + G_{ij}^n\frac{\partial}{\partial x_j}\Delta_D(\boldsymbol{x}-\boldsymbol{Y}^n)\right\}, \tag{3}$$

where F_i and G_{ij} are the force monopole and force dipole moments, respectively. Δ_M and Δ_D are the FCM force envelopes defined as

$$\Delta_M(\boldsymbol{x}) = \frac{1}{(2\pi\sigma_M^2)^{3/2}}\exp\left(-\frac{\boldsymbol{x}^2}{2\sigma_M^2}\right), \tag{4}$$

$$\Delta_D(\boldsymbol{x}) = \frac{1}{(2\pi\sigma_D^2)^{3/2}}\exp\left(-\frac{\boldsymbol{x}^2}{2\sigma_D^2}\right). \tag{5}$$

The length scales σ_M and σ_D are chosen to satisfy the overall energy budget for the flow [11,12],

$$\frac{a}{\sigma_M} = \sqrt{\pi}, \tag{6}$$

$$\frac{a}{\sigma_D} = \left(6\sqrt{\pi}\right)^{1/3}. \tag{7}$$

These expressions for the length scales ensure that the exact Stokes drag is obtained and further that corresponding degenerate force quadrupoles, the linear Faxen terms for finite particle size and local flow variations are estimated with no additional terms.

Once $\boldsymbol{u}(\boldsymbol{x})$ is obtained, the velocity of each particle $\boldsymbol{V}^n(t)$ is found by the weighted volume integral of $\boldsymbol{u}(\boldsymbol{x})$ [11],

$$\boldsymbol{V}^n = \int\boldsymbol{u}(\boldsymbol{x})\Delta_M(\boldsymbol{x}-\boldsymbol{Y}^n)d^3\boldsymbol{x}. \tag{8}$$

Similarly, the angular velocity of each particle $\boldsymbol{\Omega}^n$ is calculated from

$$\boldsymbol{\Omega}_i^n = \frac{1}{2}\int\epsilon_{ijk}\frac{\partial u_k}{\partial x_j}\Delta_D(\boldsymbol{x}-\boldsymbol{Y}^n)d^3\boldsymbol{x}. \tag{9}$$

The monopole coefficient $\boldsymbol{F}^n$ is the force of the particle on the fluid, which is the sum of forces on the particle other than the hydrodynamic interaction, and include gravity, short-range inter-particle surface forces, magnetic forces, and random Brownian forces.

The dipole coefficient G_{ij} consists of symmetric and anti-symmetric parts. The anti-symmetric part T_{ij} is related to the torque exerted by the particle on the fluid,

$$T_{ij} = \frac{1}{2}\epsilon_{ijk}T_k^{ext}, \tag{10}$$

in which $\boldsymbol{T}^{ext}$ in turn denotes an external torque on the particle. The symmetric part S_{ij} corresponds to a stresslet acting on the fluid. S_{ij} is found from the condition that the contribution of the stresslet to the total rate of work on the fluid is zero [12]. In other words, S_{ij} is chosen to satisfy the constraint,

$$E_{ij} = \frac{1}{2}\int\left(\frac{\partial u_i}{\partial x_j}+\frac{\partial u_j}{\partial x_i}\right)\Delta_D(\boldsymbol{x}-\boldsymbol{Y}^n(t))d^3\boldsymbol{x} = 0, \tag{11}$$

for each particle. Since S_{ij} depends on the rate-of-strain, it has to be determined by an iterative method. Lomholt et al. [29] and Dance and Maxey [36] described steepest-decent iterative methods to accomplish this.

2.2. Discretized equation of FCM

Due to the linearity of the Stokes equation, there are linear relations between the force moments and the flow parameters [38,39]. Finding the force moments from the prescribed flow parameters is called the resistance problem while in the mobility problem the flow parameters are the unknowns which are to be found from the given force moments. In this section, the semi-discretized equation of the force-coupling method is presented conceptually in the form of the grand mobility matrix and a more efficient conjugate gradient method to calculate S_{ij} is described.

For simplicity, let the computational domain $\mathbf{\Omega}^D$ be a cubic domain in $\mathbb{R}^3$. $\mathbf{\Omega}^D$ can be a bounded domain with some boundary conditions on $\partial\mathbf{\Omega}^D$ or an unbounded domain with periodic boundary conditions. We consider the fluid of a constant viscosity μ extends in the whole domain including the volume occupied by the particles and the fluid velocity and pressure satisfy Eqs. (1), (2) in $\mathbf{\Omega}^D$.

In Eq. (8), $\boldsymbol{V}^n$ can be approximated by a Gaussian quadrature rule,

$$\boldsymbol{V}^n = \sum_{i=1}^{N_x}\sum_{j=1}^{N_y}\sum_{k=1}^{N_z} \boldsymbol{u}(\boldsymbol{x}^{i,j,k})\Delta_M(\boldsymbol{x}^{i,j,k} - \boldsymbol{Y}^{\,n})w_i^x w_j^y w_k^z, \tag{12}$$

in which N_x, N_y, and N_z are, respectively, the number of grid points in the x_1, x_2, and x_3 directions (or x, y, z), $\boldsymbol{x}^{i,j,k}$ is the position vector of the (i,j,k)th grid point, and w_i^α is the weight of the Gaussian quadrature in the α direction. In matrix form,

$$\boldsymbol{V} = \boldsymbol{D_M W u}, \tag{13}$$

in which the terms are

$\boldsymbol{V}$: $(3N_p)$ vector which contains the particle velocities

$$\boldsymbol{V} = \begin{bmatrix} \boldsymbol{V}_1 \\ \boldsymbol{V}_2 \\ \boldsymbol{V}_3 \end{bmatrix}, \quad \boldsymbol{V}_j = \begin{bmatrix} V_j^1 \\ V_j^2 \\ \vdots \\ V_j^{N_p} \end{bmatrix}. \tag{14}$$

$\boldsymbol{u}$: $(3Ng)$ vector for the fluid velocity at each grid points $(Ng = N_x \times N_y \times N_z)$.

$$\boldsymbol{u} = \begin{bmatrix} \boldsymbol{u}_1 \\ \boldsymbol{u}_2 \\ \boldsymbol{u}_3 \end{bmatrix}, \quad \boldsymbol{u}_j = \begin{bmatrix} u_j(\boldsymbol{x}^{1,1,1}) \\ \vdots \\ u_j(\boldsymbol{x}^{N_x,N_y,N_z}) \end{bmatrix}. \tag{15}$$

$\boldsymbol{W}$: $(3Ng) \times (3Ng)$ diagonal matrix for the weighting coefficients of the Gaussian quadrature.

$$\boldsymbol{W} = \begin{bmatrix} \boldsymbol{w} & \boldsymbol{0} & \boldsymbol{0} \\ \boldsymbol{0} & \boldsymbol{w} & \boldsymbol{0} \\ \boldsymbol{0} & \boldsymbol{0} & \boldsymbol{w} \end{bmatrix}, \quad \boldsymbol{w} = \begin{bmatrix} w_1^x w_1^y w_1^z & 0 & \cdots & 0 \\ 0 & \ddots & & \vdots \\ \vdots & & \ddots & 0 \\ 0 & \cdots & 0 & w_{N_x}^x w_{N_y}^y w_{N_z}^z \end{bmatrix}. \tag{16}$$

$\boldsymbol{D_M}$: $(3N_p) \times (3Ng)$ matrix of Δ_M at each grid points.

$$\begin{aligned} \boldsymbol{D_M} &= \begin{bmatrix} \boldsymbol{d} & \boldsymbol{0} & \boldsymbol{0} \\ \boldsymbol{0} & \boldsymbol{d} & \boldsymbol{0} \\ \boldsymbol{0} & \boldsymbol{0} & \boldsymbol{d} \end{bmatrix}, \\ \boldsymbol{d} &= \begin{bmatrix} \Delta_M(\boldsymbol{x}^{1,1,1} - \boldsymbol{Y}^{\,1}) & \cdots & \Delta_M(\boldsymbol{x}^{N_x,N_y,N_z} - \boldsymbol{Y}^{\,1}) \\ \vdots & & \vdots \\ \Delta_M(\boldsymbol{x}^{1,1,1} - \boldsymbol{Y}^{\,N_p}) & \cdots & \Delta_M(\boldsymbol{x}^{N_x,N_y,N_z} - \boldsymbol{Y}^{\,N_p}) \end{bmatrix} \end{aligned} \tag{17}$$

It is worthwhile to note that, because the force envelope is a rapidly decaying function, we can assume $\Delta_M(\boldsymbol{x} - \boldsymbol{Y}) = 0$ if $|\boldsymbol{x} - \boldsymbol{Y}| > 3a$, which makes $\boldsymbol{d}$ a sparse matrix. Hence, the matrix–matrix multiplication $\boldsymbol{D_M W u}$ is done in $O(N_p)$ operations.

Through linearity, the flow parameters can be represented by the sum of their components. First, the fluid velocity $\boldsymbol{u}$ generated by the given force monopole is

$$\boldsymbol{u} = \mathbb{S}\boldsymbol{D}_{\boldsymbol{M}}^{T}\boldsymbol{F}, \tag{18}$$

in which $\mathbb{S}$ is a $(3Ng) \times (3Ng)$ matrix determined by the choice of a numerical scheme to solve the Stokes equations and $\boldsymbol{F}$ is the $3N_p$ vector containing the monopole coefficients of each particle.

$$\boldsymbol{F} = \begin{bmatrix} \boldsymbol{f}_1 \\ \boldsymbol{f}_2 \\ \boldsymbol{f}_3 \end{bmatrix}, \quad \boldsymbol{f}_j = \begin{bmatrix} F_j^1 \\ \vdots \\ F_j^{N_p} \end{bmatrix} \tag{19}$$

In terms of these, the particle velocity $\boldsymbol{V}$ from the FCM monopole calculation is

$$\boldsymbol{V} = \boldsymbol{D_M} \boldsymbol{W} \mathbb{S} \boldsymbol{D_M^T} \boldsymbol{F} = \boldsymbol{M_{FV}} \boldsymbol{F}, \tag{20}$$

in which $\boldsymbol{M_{FV}}$ is the FCM mobility matrix relating the translational velocity to the force monopole. In the Stokes problem, the symmetric positive definiteness (SPD) of the mobility matrix can be proven by the reciprocal theorem [39]. The same property is preserved in FCM. It is trivial to show that the positive semi-definiteness of $\mathbb{S}$, which is true for many numerical schemes such as the spectral or the spectral element methods, implies the positive semi-definiteness of $\boldsymbol{M_{FV}}$.

Secondly, the mobility matrix for the rate-of-strain (11) in response to the symmetric force dipole (stresslet) is similarly given by

$$\boldsymbol{M_{SE}} = -\boldsymbol{D_D} \boldsymbol{W} \mathbb{S} \boldsymbol{D_D^T}, \tag{21}$$

in which $\boldsymbol{D_D}$ is a $(5N_p) \times (3Ng)$ matrix to calculate the derivatives of the dipole Gaussian envelope $\Delta_D(\boldsymbol{x} - \boldsymbol{Y})$,

$$\begin{aligned} \boldsymbol{D_D} &= \begin{bmatrix} \boldsymbol{d_x} & \boldsymbol{0} & -\boldsymbol{d_z} \\ \boldsymbol{d_y} & \boldsymbol{d_x} & \boldsymbol{0} \\ \boldsymbol{d_z} & \boldsymbol{0} & \boldsymbol{d_x} \\ \boldsymbol{0} & \boldsymbol{d_y} & -\boldsymbol{d_z} \\ \boldsymbol{0} & \boldsymbol{d_z} & \boldsymbol{d_y} \end{bmatrix}, \\ \boldsymbol{d_x} &= \begin{bmatrix} \frac{\partial}{\partial x}\Delta_D(\boldsymbol{x}^{1,1,1} - \boldsymbol{Y}^{\ 1}) & \cdots & \frac{\partial}{\partial x}\Delta_D(\boldsymbol{x}^{N_x,N_y,N_z} - \boldsymbol{Y}^{\ 1}) \\ \vdots & & \vdots \\ \frac{\partial}{\partial x}\Delta_D(\boldsymbol{x}^{1,1,1} - \boldsymbol{Y}^{\ N_p}) & \cdots & \frac{\partial}{\partial x}\Delta_D(\boldsymbol{x}^{N_x,N_y,N_z} - \boldsymbol{Y}^{\ N_p}) \end{bmatrix}. \end{aligned} \tag{22}$$

Here, a derivative of $\boldsymbol{u}$ is calculated by

$$\int \frac{\partial u_i}{\partial x_j} \Delta_D(\boldsymbol{x} - \boldsymbol{Y}) d^3\boldsymbol{x} = -\int u_i \frac{\partial}{\partial x_j} \Delta_D(\boldsymbol{x} - \boldsymbol{Y}) d^3\boldsymbol{x}. \tag{23}$$

Eq. (23) holds when either $\boldsymbol{u}$ or Δ_D has compact support in $\boldsymbol{\Omega}^D$. In a bounded domain, although Δ_D is not compact in $\boldsymbol{\Omega}^D$, $\boldsymbol{u}$ vanishes on $\partial\boldsymbol{\Omega}^D$. Therefore, Eq. (23) holds also for the bounded domain.

Instead of calculating all nine components of the rate-of-strain E_{ij}, only five independent components are evaluated

$$\widetilde{\boldsymbol{E}} = \begin{bmatrix} \boldsymbol{E}_{11} - \boldsymbol{E}_{33} \\ 2\boldsymbol{E}_{12} \\ 2\boldsymbol{E}_{13} \\ \boldsymbol{E}_{22} - \boldsymbol{E}_{33} \\ 2\boldsymbol{E}_{23} \end{bmatrix}. \tag{24}$$

Similarly, let $\boldsymbol{D_T}$ be a $(3N_p) \times (3Ng)$ matrix whose entries are

$$\boldsymbol{D_T} = \frac{1}{2} \begin{bmatrix} \boldsymbol{0} & \boldsymbol{d_z} & -\boldsymbol{d_y} \\ -\boldsymbol{d_z} & \boldsymbol{0} & \boldsymbol{d_x} \\ \boldsymbol{d_y} & -\boldsymbol{d_x} & \boldsymbol{0} \end{bmatrix}. \tag{25}$$

Then, the mobility matrix for the angular velocity of particles in response to torque is given as

$$\boldsymbol{M_{T\Omega}} = \boldsymbol{D_T} \boldsymbol{W} \mathbb{S} \boldsymbol{D_T^T}. \tag{26}$$

The definitions of the other mobility matrices are as follows:

$$\boldsymbol{M_{TV}} = \boldsymbol{D_M} \boldsymbol{W} \mathbb{S} \boldsymbol{D_T^T}, \quad \boldsymbol{M_{SV}} = \boldsymbol{D_M} \boldsymbol{W} \mathbb{S} \boldsymbol{D_D^T}, \quad \boldsymbol{M_{S\Omega}} = \boldsymbol{D_T} \boldsymbol{W} \mathbb{S} \boldsymbol{D_D^T}. \tag{27}$$

Consistent with reciprocal theorem, the FCM mobility matrices have the following symmetry relations,

$$\boldsymbol{M_{TV}} = \boldsymbol{M_{F\Omega}^T}, \quad \boldsymbol{M_{SV}} = -\boldsymbol{M_{FE}^T}, \quad \boldsymbol{M_{S\Omega}} = -\boldsymbol{M_{TE}^T}. \tag{28}$$

Applying constraints for the stresslet coefficients (11), the FCM grand mobility matrix $\boldsymbol{M}^{FCM}$ is constructed as

$$\begin{bmatrix} \boldsymbol{V}-\boldsymbol{V}^{\infty} \\ \boldsymbol{\Omega}-\boldsymbol{\Omega}^{\infty} \\ -\widetilde{\boldsymbol{E}}^{\infty} \end{bmatrix} = \boldsymbol{M}^{FCM} \begin{bmatrix} \boldsymbol{F} \\ \boldsymbol{T} \\ \boldsymbol{S} \end{bmatrix} = \begin{bmatrix} \boldsymbol{M}_{FV} & \boldsymbol{M}_{TV} & \boldsymbol{M}_{SV} \\ \boldsymbol{M}_{F\Omega} & \boldsymbol{M}_{T\Omega} & \boldsymbol{M}_{S\Omega} \\ \boldsymbol{M}_{FE} & \boldsymbol{M}_{TE} & \boldsymbol{M}_{SE} \end{bmatrix} \begin{bmatrix} \boldsymbol{F} \\ \boldsymbol{T} \\ \boldsymbol{S} \end{bmatrix}, \tag{29}$$

in which a sub-matrix $\boldsymbol{M}_{AB}$ of $\boldsymbol{M}^{FCM}$ is a mobility matrix to calculate a value B from a given coefficient A. $\boldsymbol{\Omega}$ and $\boldsymbol{T}$ are $(3N_p)$ vectors containing the angular velocity and torques, respectively. $\boldsymbol{S}$ is a $(5N_p)$ vector of the five independent stresslet coefficients, $S_{11},\ S_{12},\ S_{13},\ S_{22},\ S_{23}$. $\boldsymbol{V}^{\infty}$ and $\boldsymbol{\Omega}^{\infty}$ are, respectively, the translational and angular velocities by imposed field. $\widetilde{\boldsymbol{E}}^{\infty}$ is the rate-of-strain vector by the imposed field. Note that the FCM grand mobility matrix in Eq. (29) is not symmetric positive semi-definite, as may be seen from Eq. (28). To make it SPD, the signs of the third row need to be changed.

Although FCM is formulated here in matrix form, in the actual computation, the grand mobility matrix need not be constructed. The computation consists of three steps:

Step 1. Calculate the force density at each grid point.

$$\boldsymbol{z} = \boldsymbol{D}_{\boldsymbol{M}}^{T}\boldsymbol{F} + \boldsymbol{D}_{\boldsymbol{T}}^{T}\boldsymbol{T} + \boldsymbol{D}_{\boldsymbol{D}}^{T}\boldsymbol{S}. \tag{30}$$

The number of operations in this step is $O(N_p)$.

Step 2. Solve the Stokes equation

$$\boldsymbol{u} = \mathbb{S}\boldsymbol{z}. \tag{31}$$

If the computational domain is periodic in all three directions, a Fourier-spectral method can be used to solve the Stokes equation. Then, the Stokes equation can be solved in $O(Ng\log(Ng))$ operations. If the domain size is increased keeping the volume fraction constant, N_p increases linearly in proportion to Ng. Hence, the number of operations in this step is $O(N_p\log(N_p))$.

Step 3. Finally, $\boldsymbol{V}$ and $\boldsymbol{\Omega}$ are computed by integrating $\boldsymbol{u}$ (Eqs. 8 and 9), which requires $O(N_p)$ operations.

As a whole, the computational cost of FCM is $O(N_p\log(N_p))$.

A key aspect of solving the flow problem is the determination of the stresslet coefficients. In Eq. (29), $\boldsymbol{F}$ and $\boldsymbol{T}$ are known while $\boldsymbol{S}$ is to be determined from the constraints for dipole moments. In other words,

$$-\widetilde{\boldsymbol{E}}^{\infty} - \boldsymbol{M}_{FE}\boldsymbol{F} - \boldsymbol{M}_{TE}\boldsymbol{T} = \boldsymbol{M}_{SE}\boldsymbol{S} \tag{32}$$

must be solved to obtain $\boldsymbol{S}$. Previously, Dance and Maxey [36] suggested a steepest-decent method to solve Eq. (32). At low volume fractions, this iterative method converges within a few iterations. However, it is found that the method converges very slowly at high volume fractions [40]. As it is shown in Eq. (21) that $-\boldsymbol{M}_{SE}$ is SPD, a conjugate gradient method can be used to solve the system [41]. The solution procedures are as follows:

Step 1. Solve the Stokes equation with $\boldsymbol{F}$, $\boldsymbol{T}$ and the initial guess $\boldsymbol{S}^0$ to calculate the residual $\boldsymbol{r}^0$ and a vector $\boldsymbol{p}^0$

$$\boldsymbol{r}^0 = \widetilde{\boldsymbol{E}}^{\infty} + \boldsymbol{D}_D\boldsymbol{W}\mathbb{S}\left(\boldsymbol{D}_M^T\boldsymbol{F} + \boldsymbol{D}_T^T\boldsymbol{T} + \boldsymbol{D}_D^T\boldsymbol{S}^0\right),$$
$$\boldsymbol{p}^0 = \boldsymbol{r}^0.$$

Step 2. Solve the Stokes equation with $\boldsymbol{p}$ as a dipole coefficient,

$$\boldsymbol{\zeta}^k = -\boldsymbol{D}_D\boldsymbol{W}\mathbb{S}\boldsymbol{D}_D^T\boldsymbol{p}^k.$$

Step 3. Update $\boldsymbol{S}$, $\boldsymbol{r}$, and $\boldsymbol{p}$ using the standard conjugate gradient procedure. Repeat the process until converges, i.e. $\|\boldsymbol{r}\| < \delta$ for a tolerance δ

$$\begin{aligned} \alpha^k &= \boldsymbol{r}^k\cdot\boldsymbol{r}^k/\boldsymbol{\zeta}^k\cdot\boldsymbol{p}^k, \\ \boldsymbol{S}^{k+1} &= \boldsymbol{S}^k + \alpha^k\boldsymbol{p}^k, \\ \boldsymbol{r}^{k+1} &= \boldsymbol{r}^k - \alpha^k\boldsymbol{\zeta}^k, \\ \beta^k &= \boldsymbol{r}^{k+1}\cdot\boldsymbol{r}^{k+1}/\boldsymbol{r}^k\cdot\boldsymbol{r}^k, \\ \boldsymbol{p}^{k+1} &= \boldsymbol{r}^{k+1} + \beta^k\boldsymbol{p}^k. \end{aligned} \tag{33}$$

Step 4. Once converged, $\boldsymbol{V}$ and $\boldsymbol{\Omega}$ are found from Eq. (29).

In that the particle velocity is calculated by solving the Stokes equation instead of constructing the grand mobility matrix, the force-coupling method is a matrix-free method to solve the mobility problem. Representing the force-coupling method as a matrix-free method gives more options to improve the method. For example, it was observed that in the bimodal suspensions finding $\boldsymbol{S}$ takes more iterations than in the monodisperse suspensions to reach a converged result [32,40]. In the limit of a dilute suspension, $\boldsymbol{M}_{SE}$ is a diagonal matrix such that

$$S_{ij}^n = \frac{20}{3}\pi\mu a_n^3 E_{ij}^n, \tag{34}$$

in which a_n is the radius of the particle n. Due to the factor a_n^3 in the diagonals of $\boldsymbol{M}_{SE}$, the condition number of $\boldsymbol{M}_{SE}$ will increase approximately as the cube of the ratio of the radius of the largest particle to the radius of the smallest particle, $\mathscr{K}(\boldsymbol{M}_{SE}) \sim (a_L/a_S)^3$, which makes it difficult to invert $\boldsymbol{M}_{SE}$ using CG even at low volume fractions. In this case, a preconditioned conjugate gradient method (PCG) is more effective [41]. From the result in the dilute limit, we can choose the preconditioner as a diagonal matrix of which elements are $3/20\pi\mu a_n^3$. Fig. 1 shows the residual L_2-norm history for a bimodal suspension in a Poiseuille flow. The size ratio (a_L/a_S) is 2 and the volume fractions of large and small particles are 9% ($N_p = 64$) and 1% ($N_p = 57$), respectively. The particles are randomly distributed. As expected, PCG converges faster than CG.

3. Lubrication correction for the force-coupling method

$\boldsymbol{M}^{FCM}$ resolves terms up to the dipole moments and the many-body interactions are naturally resolved by solving the Stokes equation. However, due to the lack of high-order terms, the force-coupling method cannot fully resolve the particle–particle interaction when the separation distance between two nearby particles is small [11,12].

Dance and Maxey [36] developed an efficient lubrication model by comparing the exact resistance relations to the numerical resistance relations of FCM for particle–pair and particle–wall interactions. The lubrication model is suited to dilute system in which most lubrication interactions come from particle doublets. To account for the multi-body lubrication interactions, the lubrication force estimated by the sum of each particle–pair interactions is added to the mobility problem as a feedback force. However, it turned out that simply adding the lubrication force to the mobility problem in a pairwise manner is not enough to resolve the many-body hydrodynamic interactions accurately [15,36].

3.1. Lubrication correction method

Since Durlofsky et al. [15] suggested a lubrication approximation scheme for their Stokesian Dynamics simulation, their approach has been successfully applied in many subsequent SD simulations [4,42,18] as well as in other simulation methods [9,6,16]. Instead of adding high-order multipole moments in the resistance matrix, they added the near-field interaction to the inverse of the grand mobility matrix in a pairwise manner as an approximation to the exact grand resistance matrix. The near-field resistance function is calculated by subtracting the two-body SD resistance matrix $\left(\boldsymbol{R}_2^{SD}\right)$ from the exact one $(\boldsymbol{R}_2)$ obtained from the lubrication theory. Considering that $\boldsymbol{L} = \boldsymbol{R}_2 - \boldsymbol{R}_2^{SD}$ contains the contributions from only high-order multipole moments which decay rapidly in space, the pairwise additivity of the lubrication correction is a reasonable approximation. In this section, we develop the lubrication correction method for the force-coupling method based on the pairwise addition of the lubrication matrix.

The FCM resistance relation is

$$(\boldsymbol{M}^{FCM})^{-1}\begin{bmatrix} \mathscr{V} - \mathscr{V}^{\infty} \\ -\widetilde{\boldsymbol{E}}^{\infty} \end{bmatrix} = \begin{bmatrix} \mathscr{F} \\ \boldsymbol{S} \end{bmatrix}, \tag{35}$$

in which

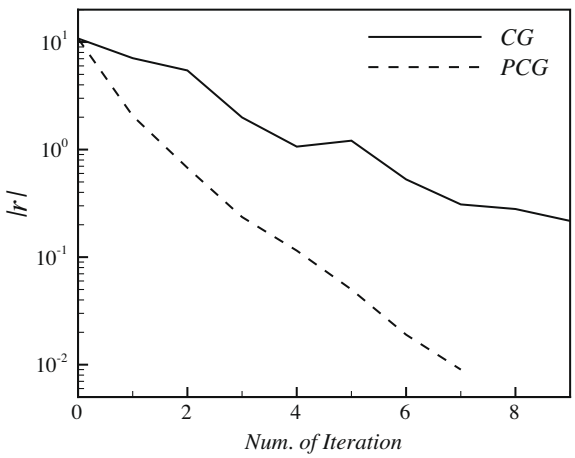

Fig. 1. The residual 2-norm history for bidisperse suspension.

$$\mathscr{V} = \begin{bmatrix} \boldsymbol{V} \\ \boldsymbol{\Omega} \end{bmatrix}, \mathscr{F} = \begin{bmatrix} \boldsymbol{F} \\ \boldsymbol{T} \end{bmatrix}. \tag{36}$$

Following [15], the resistance matrix with the lubrication correction is

$$((\boldsymbol{M}^{FCM})^{-1} + \boldsymbol{L}) \begin{bmatrix} \mathscr{V} - \mathscr{V}^{\infty} \\ -\widetilde{\boldsymbol{E}}^{\infty} \end{bmatrix} = \begin{bmatrix} \mathscr{F} \\ \boldsymbol{S} \end{bmatrix}, \tag{37}$$

in which the lubrication correction matrix $\boldsymbol{L}$ is

$$\boldsymbol{L} = \begin{bmatrix} \boldsymbol{R}^L_{VF} & \boldsymbol{R}^L_{\Omega F} & \boldsymbol{R}^L_{EF} \\ \boldsymbol{R}^L_{VT} & \boldsymbol{R}^L_{\Omega T} & \boldsymbol{R}^L_{ET} \\ \boldsymbol{R}^L_{VS} & \boldsymbol{R}^L_{\Omega S} & \boldsymbol{R}^L_{ES} \end{bmatrix}. \tag{38}$$

$\boldsymbol{R}_{AB}$ is the resistance matrix to calculate B from given A and $\boldsymbol{R}^L$ is the difference between the exact two-body resistance matrix and the FCM resistance matrix, $\boldsymbol{R}^L = \boldsymbol{R}_{2B} - \boldsymbol{R}^{FCM}_{2B}$. Let

$$\mathscr{R} = \begin{bmatrix} \boldsymbol{R}^L_{VF} & \boldsymbol{R}^L_{\Omega F} \\ \boldsymbol{R}^L_{VT} & \boldsymbol{R}^L_{\Omega T} \end{bmatrix}. \tag{39}$$

Multiplying $\boldsymbol{M}^{FCM}$ on both sides of Eq. (37) and rearranging give

$$\begin{bmatrix} \boldsymbol{M}_{\mathscr{F}\mathscr{V}} \mathscr{F}^{tot} \\ -\boldsymbol{M}_{\mathscr{F}E} \mathscr{F}^{tot} - \widetilde{\boldsymbol{E}}^{\infty} \end{bmatrix} = \begin{bmatrix} \boldsymbol{I} + \boldsymbol{M}_{\mathscr{F}\mathscr{V}} \mathscr{R} & -\boldsymbol{M}_{S\mathscr{V}} \\ -\boldsymbol{M}_{\mathscr{F}E} \mathscr{R} & \boldsymbol{M}_{SE} \end{bmatrix} \begin{bmatrix} \mathscr{V} - \mathscr{V}^{\infty} \\ \boldsymbol{S}^{tot} \end{bmatrix}, \tag{40}$$

in which

$$\mathscr{F}^{tot} = \mathscr{F} + R^L_{E\mathscr{F}} \boldsymbol{E}^{\infty}, \tag{41}$$

$$\boldsymbol{S}^{tot} = \boldsymbol{S} + R^L_{ES} \boldsymbol{E}^{\infty} - R^L_{\mathscr{V}S} (\mathscr{V} - \mathscr{V}^{\infty}). \tag{42}$$

Note that the dipole coefficient $\boldsymbol{S}^{tot}$ obtained by solving Eq. (40) is different from the stresslet of the particle $\boldsymbol{S}$.

Eq. (40) is not SPD. So that a GMRES or bi-conjugate gradient method is required to solve the system. However, often these converge slowly or in some cases the convergence is not even guaranteed. Instead, in order to make the matrix SPD, Eq. (40) is solved for $\mathscr{F}^{lub} = \mathscr{R}(\mathscr{V} - \mathscr{V}^{\infty})$ instead of $\mathscr{V} - \mathscr{V}^{\infty}$. Rewriting Eq. (40) yields

$$\begin{bmatrix} \boldsymbol{M}_{\mathscr{F}\mathscr{V}} \mathscr{F}^{tot} \\ \boldsymbol{M}_{\mathscr{F}E} \mathscr{F}^{tot} + \widetilde{\boldsymbol{E}}^{\infty} \end{bmatrix} = \begin{bmatrix} \mathscr{R}^{-1} + \boldsymbol{M}_{\mathscr{F}\mathscr{V}} & -\boldsymbol{M}_{S\mathscr{V}} \\ \boldsymbol{M}_{\mathscr{F}E} & -\boldsymbol{M}_{SE} \end{bmatrix} \begin{bmatrix} \mathscr{F}^{lub} \\ \boldsymbol{S}^{tot} \end{bmatrix}. \tag{43}$$

The signs in the second row are changed to make the matrix symmetric.

The resistance relation for the force and torque of a particle pair is

$$\begin{bmatrix} \boldsymbol{F}^1 \\ \boldsymbol{F}^2 \\ \boldsymbol{T}^1 \\ \boldsymbol{T}^2 \end{bmatrix} = \mu \begin{bmatrix} \boldsymbol{A}^{11} & \boldsymbol{A}^{12} & \boldsymbol{B}^{11} & -\boldsymbol{B}^{12} & \boldsymbol{G}^{11} & -\boldsymbol{G}^{12} \\ \boldsymbol{A}^{12} & \boldsymbol{A}^{11} & \boldsymbol{B}^{12} & -\boldsymbol{B}^{11} & \boldsymbol{G}^{12} & -\boldsymbol{G}^{11} \\ (\boldsymbol{B}^{11})^T & (\boldsymbol{B}^{12})^T & \boldsymbol{C}^{11} & \boldsymbol{C}^{12} & \boldsymbol{H}^{11} & \boldsymbol{H}^{12} \\ -(\boldsymbol{B}^{12})^T & -(\boldsymbol{B}^{11})^T & \boldsymbol{C}^{12} & \boldsymbol{C}^{11} & \boldsymbol{H}^{12} & \boldsymbol{H}^{11} \end{bmatrix} \begin{bmatrix} \boldsymbol{V}^1 - \boldsymbol{V}^{\infty}(\boldsymbol{Y}^{\,1}) \\ \boldsymbol{V}^2 - \boldsymbol{V}^{\infty}(\boldsymbol{Y}^{\,2}) \\ \boldsymbol{\Omega}^1 - \boldsymbol{\Omega}^{\infty}(\boldsymbol{Y}^{\,1}) \\ \boldsymbol{\Omega}^2 - \boldsymbol{\Omega}^{\infty}(\boldsymbol{Y}^{\,2}) \\ -\boldsymbol{E}^{\infty} \\ -\boldsymbol{E}^{\infty} \end{bmatrix}. \tag{44}$$

Exploiting the axisymmetry of the two sphere configuration, the resistance tensors can be written in terms of several scalar functions. Following the notation in Kim and Karrila [39],

$$A^{\alpha\beta}_{ij}/6\pi a = X^A_{\alpha\beta} d_i d_j + Y^A_{\alpha\beta}(\delta_{ij} - d_i d_j),$$

$$B^{\alpha\beta}_{ij}/6\pi a^2 = Y^B_{\alpha\beta} \epsilon_{jik} d_k,$$

$$C^{\alpha\beta}_{ij}/8\pi a^3 = X^C_{\alpha\beta} d_i d_j + Y^C_{\alpha\beta}(\delta_{ij} - d_i d_j),$$

$$G^{\alpha\beta}_{kij}/6\pi a^2 = X^G_{\alpha\beta}\left(d_i d_j - \frac{1}{3}\delta_{ij}\right) d_k + Y^G_{\alpha\beta}(d_i \delta_{jk} + d_j \delta_{ik} - 2 d_i d_j d_k),$$

$$H^{\alpha\beta}_{kij}/8\pi a^3 = Y^H_{\alpha\beta}(\epsilon_{ikl} d_l d_j + \epsilon_{jkl} d_l d_i),$$

in which $\boldsymbol{d} = \boldsymbol{r}/|\boldsymbol{r}|$ and $\boldsymbol{r} = \boldsymbol{Y}^{\,\beta} - \boldsymbol{Y}^{\,\alpha}$. The analytic forms of the scalar functions are given in [36,39,43].

To calculate the FCM resistance function, first the two-particle mobility matrices for various configurations and separation distances were constructed from the FCM Oseen operator given in [11,12]. Then, the mobility matrices were inverted to obtain the values of the resistance functions for each separation distance. Finally, the resistance functions were found by a non-singular asymptotic matching,

$$R = C_0 + C_1\epsilon + C_2\epsilon^2 + C_3\epsilon^3 + C_4\epsilon^4, \tag{45}$$

in which ϵ is the separation distance between two particles, $a\epsilon = |\boldsymbol{r}| - 2a$. Coefficients of the polynomials are given in Table 1.

An example of the FCM resistance function is shown in Fig. 2. X^A_{11} is a resistance function relating the force and the translational velocity for the translational motion along the sphere–sphere axis [39]. The corresponding values of X^A_{11} for the force-torque-stresslet version of SD (SD-FTS) is obtained from [44]. For this resistance function, it is shown that the force-coupling method shows the similar far-field approximation with SD-FTS. It is shown that FCM resistance function is almost indistinguishable from the exact resistance function when $r/a > 2.5$. Hence, the cut-off distance for the lubrication interaction is set to $r_c = 2.8a$.

Solving Eq. (43) using a conjugate gradient method requires inner and outer conjugate gradient solvers to invert both $\mathscr{R}$ and the full system simultaneously. However, due to the large condition number, it is not trivial to compute $\mathscr{R}^{-1}$ using an iterative solver. For example, in a squeezing configuration of a particle pair, only the resistance function X^A is considered

$$\begin{bmatrix} F^1_{\parallel} \\ F^2_{\parallel} \end{bmatrix} = 6\pi\mu a \begin{bmatrix} X^A_{11} & X^A_{12} \\ X^A_{12} & X^A_{11} \end{bmatrix} \begin{bmatrix} V^1_{\parallel} \\ V^2_{\parallel} \end{bmatrix}. \tag{46}$$

The leading-order singular term in X^A is $1/\epsilon$ and the difference between diagonal $\left(X^A_{11}\right)$ and off-diagonal $\left(X^A_{12}\right)$ terms are $O(10^{-3})$, which makes the condition number of the matrix $\mathscr{K}(\mathscr{R}) \sim 1/\epsilon \times 10^3$ for ϵ small. Even when $\epsilon = 10^{-3}$, $\mathscr{K}(\mathscr{R})$ is $O(10^6)$. At high volume fractions, $\mathscr{K}(\mathscr{R})$ becomes too large for the matrix to be inverted using the standard conjugate gradient method.

Here, we present a preconditioned conjugate gradient method in which $\mathscr{R}^{-1}$ is calculated recursively without an iterative solver. Let $\boldsymbol{P}$ be a preconditioner for Eq. (43) defined as

$$\boldsymbol{P}^{-1} = \begin{bmatrix} \mathscr{R} & \boldsymbol{0} \\ \boldsymbol{0} & \kappa \boldsymbol{I} \end{bmatrix}, \tag{47}$$

in which κ is a scale factor, $\kappa = \frac{20}{3}\pi\mu a^3$. The procedure is as follows

Step 1. *Initialization*:Initialize vectors $\boldsymbol{r}, \boldsymbol{\psi}$, and $\boldsymbol{\phi}$ from an initial estimate $\mathscr{F}^0 = \mathscr{R}\mathscr{V}^0$ and $\boldsymbol{S}^0$.

$$\begin{bmatrix} \boldsymbol{r}^0_f \\ \boldsymbol{r}^0_s \end{bmatrix} = \begin{bmatrix} \boldsymbol{M}_{\mathscr{F}\mathscr{V}}(\mathscr{F}^{tot} - \mathscr{F}^0) + \boldsymbol{M}_{S\mathscr{V}}\boldsymbol{S}^0 - \mathscr{V}^0 \\ \boldsymbol{M}_{\mathscr{F}E}(\mathscr{F}^{tot} - \mathscr{F}^0) + \boldsymbol{M}_{SE}\boldsymbol{S}^0 + \widetilde{\boldsymbol{E}}^{\infty} \end{bmatrix}, \tag{48}$$

$$\begin{bmatrix} \psi^0_f \\ \psi^0_s \end{bmatrix} = \boldsymbol{P}^{-1}\boldsymbol{r}^0 = \begin{bmatrix} \mathscr{R}\boldsymbol{r}^0_f \\ \kappa \boldsymbol{r}^0_s \end{bmatrix}, \tag{49}$$

$$\boldsymbol{\phi}^0 = \boldsymbol{\psi}^0. \tag{50}$$

Table 1
FCM resistance functions.

	C_0	C_1	C_2	C_3	C_4
X^A_{11}	2.3593	−2.6950	3.4626	−2.6058	0.8310
X^A_{12}	−1.7187	2.7545	−3.4658	2.6047	−0.8308
X^C_{11}	1.0151	−0.0419	0.0576	−0.0426	0.0132
X^C_{12}	−0.1241	0.1783	−0.1524	0.0816	−0.0205
X^G_{11}	0.9670	−2.0276	2.4960	−1.7932	0.5540
X^G_{12}	−1.1651	2.0898	−2.5005	1.7946	−0.5563
Y^A_{11}	1.3351	−0.6292	0.7689	−0.5602	0.1754
Y^A_{12}	−0.6114	0.7157	−0.7830	0.5571	−0.1737
Y^B_{11}	−0.1998	0.4427	−0.5613	0.4066	−0.1256
Y^B_{12}	0.3532	−0.5293	0.5749	−0.3972	0.1238
Y^C_{11}	1.1253	−0.3090	0.3944	−0.2779	0.0832
Y^C_{12}	0.0965	−0.1827	0.2050	−0.1378	0.0409
Y^G_{11}	0.0816	−0.2134	0.2889	−0.2144	0.0668
Y^G_{12}	−0.1111	0.2423	−0.2936	0.2065	−0.0630
Y^H_{11}	0.0165	−0.0669	0.1117	−0.0909	0.0294
Y^H_{12}	0.1695	−0.2605	0.2386	−0.1362	0.0361

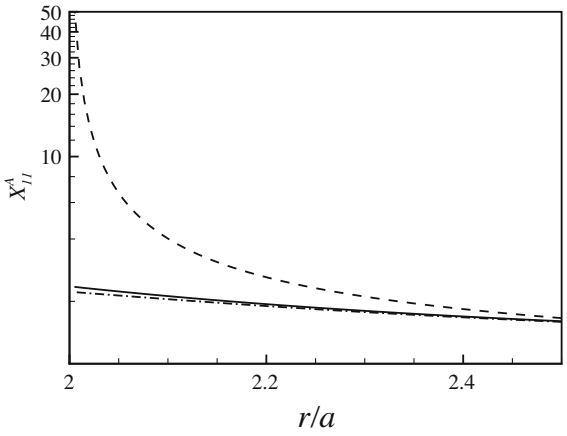

Fig. 2. The resistance function X^A_{11} of the exact solution (dashed line), FCM (solid line), and SD-FTS (dash-dot line).

Step 2. *Iteration*: For $n = 0, 1, \ldots$

$$\alpha^n = \frac{\boldsymbol{\psi}^n \cdot \boldsymbol{r}^n}{\boldsymbol{\phi}^n \cdot \boldsymbol{A}\boldsymbol{\phi}^n} \tag{51}$$

$$\begin{bmatrix} \mathscr{F}^{n+1} \\ \boldsymbol{S}^{n+1} \end{bmatrix} = \begin{bmatrix} \mathscr{F}^{n} \\ \boldsymbol{S}^{n} \end{bmatrix} + \alpha^n \begin{bmatrix} \phi_f^n \\ \phi_s^n \end{bmatrix}, \tag{52}$$

$$\boldsymbol{r}^{n+1} = \boldsymbol{r}^n - \alpha^n \boldsymbol{A}\boldsymbol{\phi}^n, \tag{53}$$

$$\boldsymbol{\psi}^{n+1} = \boldsymbol{P}^{-1}\boldsymbol{r}^{n+1}, \tag{54}$$

$$\beta^n = \frac{\boldsymbol{\psi}^{n+1} \cdot \boldsymbol{r}^{n+1}}{\boldsymbol{\psi}^n \cdot \boldsymbol{r}^n}, \tag{55}$$

$$\boldsymbol{\phi}^{n+1} = \boldsymbol{\psi}^{n+1} + \beta^n \boldsymbol{\phi}^n, \tag{56}$$

where

$$\boldsymbol{A} = \begin{bmatrix} \mathscr{R}^{-1} + \boldsymbol{M}_{\mathscr{F}\mathscr{V}} & -\boldsymbol{M}_{S\mathscr{V}} \\ \boldsymbol{M}_{\mathscr{F}E} & -\boldsymbol{M}_{SE} \end{bmatrix}. \tag{57}$$

Step 3. Repeat step 2 until $\|\boldsymbol{r}^{n+1}\|^2 \leqslant \delta$ for a tolerance level δ.

In step 2, $\boldsymbol{A}\boldsymbol{\phi}^n$ involves computing $\mathscr{R}^{-1}\phi_f^n$. From the initialization step, it is obvious that

$$\mathscr{R}^{-1}\phi_f^0 = \mathscr{R}^{-1}\psi_f^0 = \boldsymbol{r}_f^0. \tag{58}$$

Similarly, for $n \geqslant 1$, there is a general recursive solution,

$$\mathscr{R}^{-1}\phi_f^n = \mathscr{R}^{-1}\left(\psi_f^n + \beta^{n-1}\phi_f^{n-1}\right) = \boldsymbol{r}_f^n + \beta^{n-1}\left(\mathscr{R}^{-1}\phi_f^{n-1}\right) = \boldsymbol{r}_f^n + \sum_{i=0}^{n-1}\left(\prod_{j=i}^{n-1}\beta^j\right)\boldsymbol{r}_f^i. \tag{59}$$

Once $\mathscr{F}^{lub}$ is found, $\mathscr{V}$ can be computed from either

$$\mathscr{V} = \mathscr{V}^{\infty} + \mathscr{R}^{-1}\mathscr{F}^{lub}, \tag{60}$$

or

$$\mathscr{V} = \mathscr{V}^{\infty} + \boldsymbol{M}_{\mathscr{F}\mathscr{V}}(\mathscr{F}^{tot} - \mathscr{F}^{lub}) + \boldsymbol{M}_{S\mathscr{V}}\boldsymbol{S}^{tot}. \tag{61}$$

Note that at low volume fractions, there are many particles which do not have particles in their neighborhood. In that case, the number of degrees of freedom of Eq. (60) is $6 \times N_c$ and not $6 \times N_p$, in which N_c denotes the number of particles which have at least one particle within the cut-off distance ($r_c = 2.8a$). Therefore, to calculate $\mathscr{V}$ for those particles which do not have any neighboring particles, we need to solve Eq. (61).

4. Results I: particles in an infinite domain

To verify the lubrication correction method developed in Section 3, several numerical simulations of spheres in an infinite domain are performed. The FCM mobility matrix is constructed by using the FCM Oseen tensors derived in [12].

4.1. Chain of particles settling under gravity

First, consider two horizontally separated spheres settling under gravity (see inset of Fig. 3). The hydrodynamic interaction induces counter-rotation of the particle pair. Near contact, the counter-rotation is frozen by the lubrication forces. The angular velocity calculated from the present lubrication correction (FCM-LUB) and FCM with just monopole and dipole terms (FCM-MD) are shown in Fig. 3. It is shown that the present lubrication correction method can reproduce the angular velocity with good accuracy when $r/a < 2.25$. At $r = 2.1$, the angular velocity obtained by Ganatos *et al.* [45] is 0.137 and the present method gives 0.139. For the resistance functions that have a leading-order $\log\epsilon$ singularity (Y^A, Y^B, Y^C, Y^G, and Y^H), the near-field form is used only when $\epsilon < 0.05$ and the far-field form is used for $0.05 < \epsilon < 0.8$. The exact resistance functions can be found in [36,43,39].

In a second example, the settling of a horizontal chain of seven spheres is calculated using FCM-LUB. The configuration of the particles is illustrated in Fig. 4 with the relative gap between the particles $\epsilon = 0.005$. The drag coefficient λ and angular velocity Ω for each particle are compared to those obtained by Ganatos et al. [45] and FTS-SD [15]. The results are shown in Fig. 5. FCM with the present lubrication correction shows similar accuracy as FTS-SD. For the drag coefficient the maximum difference of λ between FCM-LUB and [45] is about 1%. The lubrication model of [36] shows relatively larger error, particularly for the particle 3. It was noted that the error at particle 3 may come from the pair-wise addition of the lubrication force in the mobility problem. This is consistent with the argument of Durlofsky et al. [15] that adding lubrication correction terms to the resistance matrix in a pair-wise manner and inverting the resistance matrix to solve the mobility problem better resolves many-body interactions as compared to adding the lubrication forces to the mobility problem.

4.2. Particles in a pure straining field

The interactions of a particle–pair in a linear flow field can be evaluated analytically and there are many solutions available in the literature [39,46,47], which are suitable for benchmarking a numerical scheme. In this section, the numerical computations for a pair of force-free and torque-free spheres in a pure straining flow are performed and the results are compared with the analytical solutions.

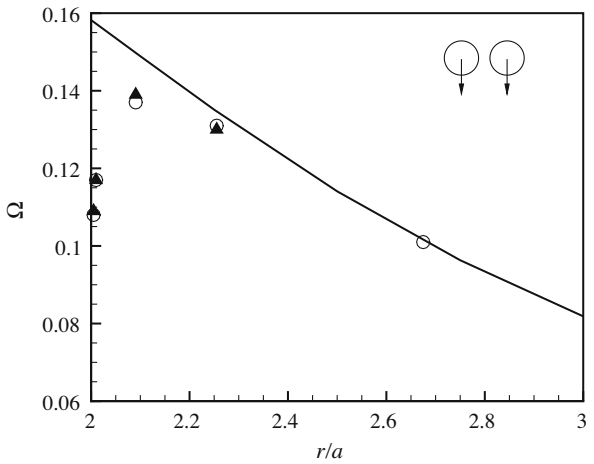

Fig. 3. Comparison of angular velocity for a pair of equal spheres with horizontal separation. ○, Ganatos et al. (1978); ▲, FCM-LUB; –, FCM-MD.

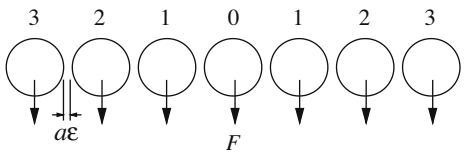

Fig. 4. Illustration of the horizontal chain of seven spheres.

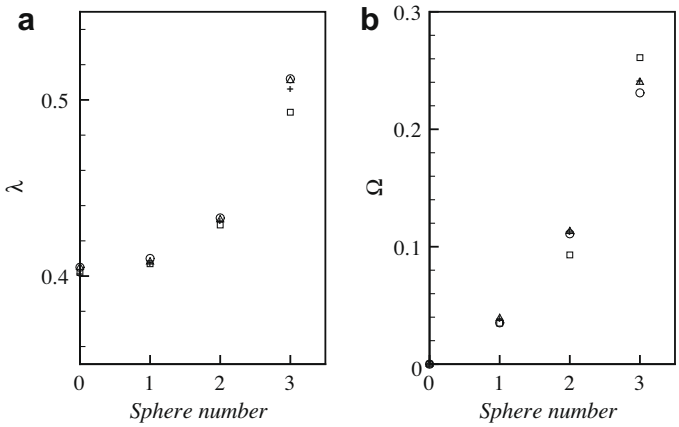

Fig. 5. Comparison of (a) the drag coefficient $\lambda = F/6\pi\mu aU$ and (b) angular velocity. ○, Ganatos et al. (1978); △, Durlofsky et al. (1987); +, FCM-LUB; □, Dance and Maxey (2003).

Consider a particle pair in a uniform straining flow (see Fig. 6),

$$E_{ij}^{\infty} = E\delta_{ij11} - \frac{1}{2}E(\delta_{ij22} + \delta_{ij33}), \tag{62}$$

$$u_i^{\infty} = E_{ij}^{\infty} x_j, \tag{63}$$

in which δ_{ijkl} is 1 if all the indices are the same and 0 otherwise. Batchelor and Green (B&G) [47] solved this problem analytically by using bispherical harmonics. When $r_i = r\delta_{i1}$ and ϵ is small, the relative velocity and stresslet in B&G are

$$V_r = (1 - A(r))Er, \tag{64}$$

$$S_{11} = \frac{20}{3}\pi\mu a^3 E\left(1 + K + \frac{4}{3}L + \frac{2}{3}M\right), \tag{65}$$

in which

$$A(r) = 1 - 4.077\epsilon + O(\epsilon^{3/2}), \tag{66}$$

$$\frac{3}{2}K + 2L + M = 1.366 + O(\epsilon). \tag{67}$$

The relative velocities from B&G and FCM-LUB are shown in Table 2. At $\epsilon = 10^{-2}$, the error is about 7%. However, due to the $O(\epsilon^{3/2})$ error of $A(r)$ in B&G, it is difficult to assess the error of numerical method at this separation distance. As ϵ decreases, the difference between B&G and the present simulation becomes smaller. When $\epsilon = 10^{-3}$, the difference between B&G and FCM-LUB is about 1%.

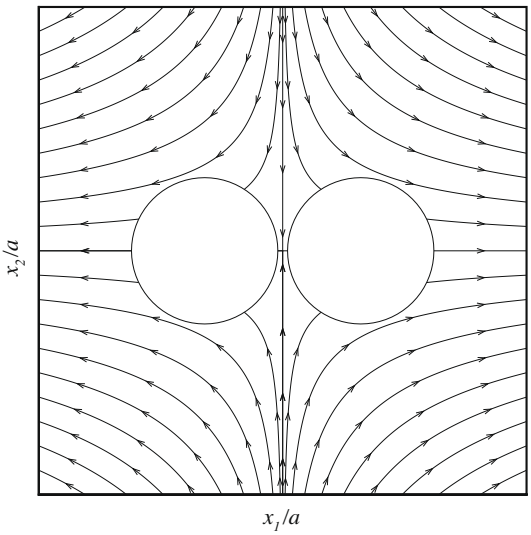

Fig. 6. Illustration of a particle–pair in a pure straining flow.

Table 2
Relative velocity of two spheres in a straining flow when $E = 1$.

ϵ	B&G	FCM
0.01	0.08195	0.07647
0.005	0.04087	0.03931
0.001	0.008158	0.008071

The stresslet of a sphere is calculated from Eq. (42),

$$\boldsymbol{S} = \boldsymbol{S}^{tot} - R^L_{ES}\boldsymbol{E}^{\infty} + R^L_{\mathscr{V}S}(\mathscr{V} - \mathscr{V}^{\infty}), \tag{68}$$

in which $R^L_{\mathscr{V}S} = -\left(R^L_{E\mathscr{F}}\right)^T$. $\boldsymbol{S}^{tot}$ is obtained by solving the Eq. (40). To estimate $\boldsymbol{S}$, the fourth-order tensor R^L_{ES} needs to be constructed. The FCM resistance functions X^M, Y^M, and Z^M are given in Table 3.

The stresslet given in B&G is

$$S_{11} = 40.017a^3E + O(\epsilon). \tag{69}$$

Using the lubrication correction, FCM gives $S_{11} = 39.226a^3E$ and $39.582a^3E$ when $\epsilon = 0.01$ and 0.005, respectively. As expected, the results get closer to B&G as ϵ decreases, and the differences are consistent with an $O(\epsilon)$ scaling.

4.3. Relative motion of a particle pair in a linear shear flow

If the surface of spheres are perfectly smooth and the interaction between a particle–pair is from purely hydrodynamics, the trajectories of the particle–pair should be time reversible as a consequence of the linearity of the Stokes equations. Consider a particle–pair in a shear flow, $u_1^{\infty}(y) = \dot{\gamma}y$, in which $\dot{\gamma}$ is a shear rate, with the initial center-to-center distances $\Delta x^I = \delta_x$, $\Delta y^I = \delta_y$, and $\Delta z^I = \delta_z$. Then, at the downstream location $\Delta x^F = -\delta_x$, the center-to-center distances in y- and z-directions should be $\Delta y^F = \delta_y$ and $\Delta z^F = \delta_z$. If δ_y and δ_z are small, the minimum separation distance during a tumbling motion of the particle pair can be very small. Da Cunha and Hinch [48] observed that for $\delta_x/a = 10$, $\delta_y/a = \delta_z/a = 0.1$, the minimum separation is $4.75 \times 10^{-5}a$. In physical systems, however, the surface roughness of particles breaks the reversibility, resulting in a net drift after the "collision". Smart and Leighton [49] measured the surface roughness of particles ranging from 43 to 6350 μm in diameter and found these to be the order of 10^{-2}–$10^{-3}a$.

Corresponding numerical simulations of a particle–pair in a linear shear flow are performed. $\delta_x/a = -10$ and $\delta_z/a = 0$ are used for all simulations. The time advancement was carried out by using a fourth-order Adam-Bashforth method with time step size $dt = 10^{-3}$. To prevent any overlap, an elastic contact force proposed by Dance et al. [30] is used. The contact force to the jth particle by the ith particle is given by

$$\boldsymbol{F}^{ij} = \begin{cases} -F_{ref}\left(\frac{R^2_{ref} - |\boldsymbol{r}|^2}{R^2_{ref} - 4a^2}\right)^2 \frac{\boldsymbol{r}}{|\boldsymbol{r}|} & \text{if } |\boldsymbol{r}| < R_{ref} \\ 0 & \text{otherwise,} \end{cases} \tag{70}$$

in which $\boldsymbol{r} = \boldsymbol{Y}^i - \boldsymbol{Y}^j$. Although in most numerical simulations a contact force is used to prevent the overlapping of particles as a result of finite dt, physically the use of a contact force is to model the surface roughness of particles [48].

Fig. 7 shows the relative trajectories and the separation distances of the two equal spheres in the shear flow for $\Delta y^I/a = 0.2,\ 0.4,\ 0.6,$ and 0.7 when $R_{ref} = 2.001$. When $\Delta y^I/a = 0.7$, the minimum separation is $\epsilon_{min} \simeq 0.0015$. Since the contact force is not activated, the trajectory shows the fore-after symmetry. For $\Delta y^I/a \leqslant 0.6$, it is observed that the symmetry is broken and there is a net displacement in the vertical direction. From the Table 4, it can be deduced that Δy^F will be the same if $\Delta y^I/a < 0.631$. Using a traction-corrected boundary element method, Ingber et al. [19] observed that $\Delta y^F/a = 0.71$ for $\Delta y^I/a < 0.71$, when the surface roughness of a particle is $5 \times 10^{-4}a$. In their simulation, the minimum separation was $\epsilon_{min} = 1.03 \times 10^{-3}$. If $\epsilon < \epsilon_{min}$, the normal motion of a particle pair is restricted. On the other hand, in the present simulation, the contact force is activated when $\epsilon < 10^{-3}$ and $\epsilon_{min} \simeq 0.97 \times 10^{-3}$, which may contribute to the quantitative difference.

Table 3
FCM resistance functions (X^M, Y^M, Z^M).

	C_0	C_1	C_2	C_3	C_4
X^M_{11}	−1.4235	0.9133	−1.0670	0.7197	−0.2120
X^M_{12}	−0.5911	0.9453	−0.9702	0.6307	−0.1852
Y^M_{11}	−1.0787	0.1991	−0.2617	0.1902	−0.0584
Y^M_{12}	0.0806	0.0370	−0.1294	0.0990	−0.0283
Z^M_{11}	−1.0035	0.0145	−0.0253	0.0221	−0.0075
Z^M_{12}	0.0593	−0.1281	0.1400	−0.0855	0.0229

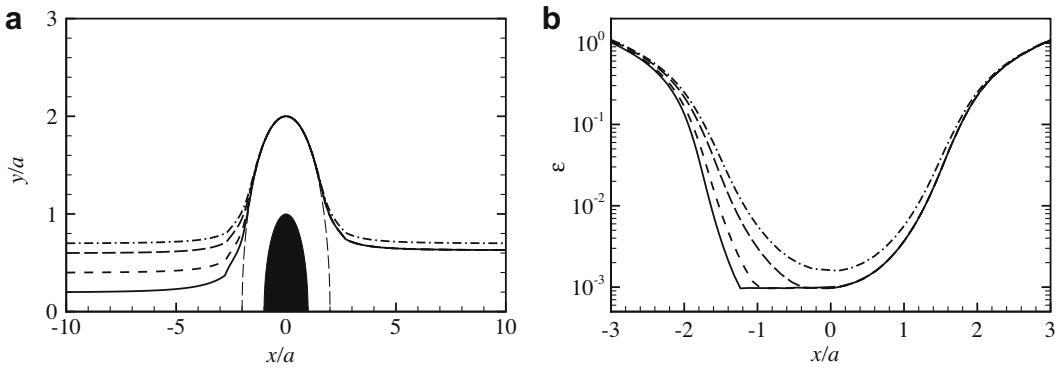

Fig. 7. (a) Relative trajectory of the centers of two equal spheres and (b) separation distances for different initial positions, Δy^I. The length scale of the contact force $R_{ref} = 2.001a$. From top to bottom: $\Delta y^I = 0.7,\ 0.6,\ 0.4,$ and 0.2.

Table 4
Upstream Δy^I and downstream center-to-center distances Δy^F for $R_{ref} = 2.001$.

$\Delta y^I/a$	$\Delta y^F/a$
0.2	0.631
0.4	0.631
0.6	0.631
0.7	0.700
0.8	0.800

The relative trajectories for $R_{ref} = 2.0001$ is illustrated in Fig. 8. It is observed that $\epsilon_{min} = 1.007783 \times 10^{-4}$ for $\Delta y^I/a = 0.2$. Since $\epsilon_{min} > R_{ref}$, the contact force is not used and the trajectories are symmetric.

5. Results II: concentrated suspensions

In this section, the numerical simulation of concentrated suspensions in a periodic cell are illustrated. Three problems are considered; a simple cubic lattice of neutrally buoyant particles, high-frequency dynamic viscosity, and sheared suspensions of non-colloidal particles. A Fourier spectral method is used to solve the Stokes equations. Periodic boundary conditions are used in all directions to model the infinite suspension. The length of the computational domain is kept constant, 2π, in all directions. The number of Fourier modes is determined by the particle radius. In FCM, as long as the force envelope is resolved the numerical result is insensitive to Δx. The computational resolution is kept $a/\Delta x \simeq 3$. The lubrication correction is used when the distance between particle centers is less than $2.8a$.

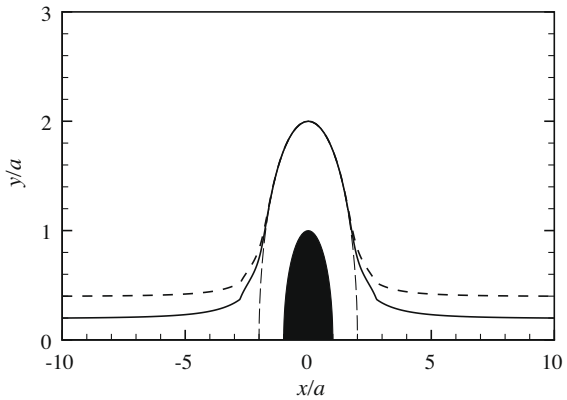

Fig. 8. Relative trajectory of the centers of two equal spheres for different initial positions, Δy^I. The length scale of the contact force is $R_{ref} = 2.0001a$. From top to bottom: $\Delta y^I = 0.4$ and 0.2.

5.1. Rheology of particles in a periodic cell

Nunan and Keller [50] showed that the bulk deviatoric stress tensor σ_{ij} is related through the effective viscosity tensor μ^*_{ijkl} to shear rate $\dot{\gamma}$ as

$$\sigma_{ij} = 2\mu^*_{ijkl}\dot{\gamma}_{kl}, \tag{71}$$

in which $\dot{\gamma}_{kl}$ denotes the shear rate. For a cubic lattice of spheres, the effective viscosity tensor is given by [50],

$$\mu^*_{ijkl} = \frac{1}{2}\mu(1+\beta)\left(\delta_{ik}\delta_{jl} + \delta_{il}\delta_{jk} - \frac{2}{3}\delta_{ij}\delta_{kl}\right) + \mu(\alpha-\beta)\left(\delta_{ijkl} - \frac{1}{3}\delta_{ij}\delta_{kl}\right), \tag{72}$$

in which α and β are functions of the volume fraction. In the case of pure straining flow, the effective viscosity tensor is a function of α only, while in the linear shear flow only β survives.

Fig. 9 shows α and β for the simple cubic lattice of neutrally buoyant particles. FCM results are compared with the low volume fraction asymptotic solution given in [50] and the high volume fraction asymptotic result by Hoffman [51]. At low ϕ where far-field interaction plays the major role, the distance between particles are larger than the cut-off distance of the lubrication correction and FCM-MD alone can reproduce the asymptotic solution. In the intermediate region, FCM-LUB predicts slightly higher effective viscosity, which is also observed in SD simulations [17]. However, the difference with the asymptotic results becomes smaller and smaller as $\phi \to \phi_{max}$.

5.2. High-frequency dynamic viscosity

The high-frequency dynamic viscosity μ^* is evaluated using the Monte Carlo approach. For each volume fraction ϕ, the shear viscosity is obtained by averaging over 1000 different random particle configurations. When $\phi \leqslant 0.35$, the random configuration can be achieved by using a uniform random number generator. For $\phi > 0.35$, body centered cubes are used initially to locate particles. Then, small random perturbations are introduced to generate the random configurations. The minimum distance between particles is kept larger than $10^{-5}a$. The contact force is not used for the Monte Carlo simulation. The simulation parameters are listed in Table 5. The number of grid points are 64^3 for all static simulations. In Fig. 10, μ^* computed by the present FCM is compared with the empirical formula by Krieger and Dougherty [52], analytical results by Batchelor and Green (B&G) [47], and the multipole-moment simulation by Ladd [6], which is used as the reference. The Stokes–Einstein estimate is obtained in the dilute regime and B&G made ϕ^2 correction in the semi-dilute regime.

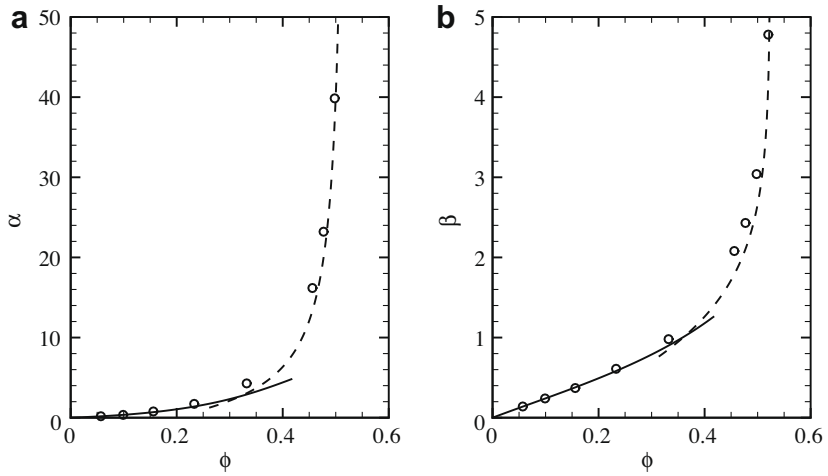

Fig. 9. The effective viscosity functions (a) α and (b) β in the functions of the volume fraction ϕ for the simple cubic lattice. The circle indicates FCM results. The dashed and solid lines are, respectively, the high and low concentration asymptotic solutions.

Table 5
Simulation parameters of the random static simulations.

ϕ	0.1	0.2	0.3	0.35	0.4	0.45	0.5
a	0.35	0.35	0.35	0.35	0.38	0.395	0.409
N_p	138	276	414	483	432	432	432

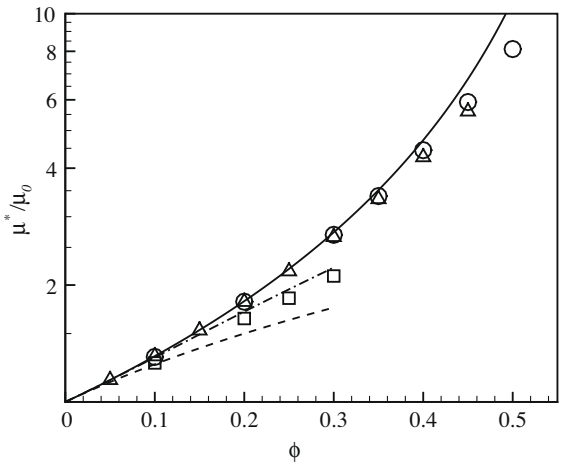

Fig. 10. Shear viscosity in terms of volume fraction. Solid line, Krieger and Dougherty (1959); dashed line, Stokes–Einstein estimate; dash-dot line, Batchelor and Green (1972); △, Ladd (1990); ○, FCM-LUB; □, FCM-MD.

1. Stokes–Einstein estimate:

$$\mu^*/\mu = 1 + \frac{5}{2}\phi. \tag{73}$$

2. Batchelor and Green (1972):

$$\mu^*/\mu = 1 + \frac{5}{2}\phi + 5.2\phi^2. \tag{74}$$

The empirical formula by Krieger and Dougherty is given by

$$\mu^*/\mu = \left(1 - \frac{\phi}{\phi_m}\right)^{-[\eta]\phi_m}, \tag{75}$$

in which ϕ_m is the maximum random packing volume fraction and $[\eta]$ is a rheological fitting parameter. Following Stickel and Powell [53], $[\eta] = \frac{5}{2}$ and $\phi_m = 0.63$ are used. It is observed that, the FCM-MD result is close to B&G. Since FCM-MD is a far-field approximation, it can reproduce the semi-dilute solution. At high ϕ, the deviation from the exact values becomes larger. It is shown that FCM-LUB gives accurate results. Although FCM-LUB predicts slightly higher μ^* compared to [6] when $\phi > 0.4$, the difference is about 5% at $\phi = 0.45$.

5.3. Sheared suspensions

Dynamic simulations are performed for $\phi = 0.3$ and 0.4. In order to impose the periodic boundary condition in conjunction with the shear flow, the computational mesh is deformed with respect to the strain ($\dot{\gamma}t$). This is done using the moving coordinate system proposed by Rogallo [54]. As the deformation of the computational mesh gets larger, more grid points are needed to integrate the force envelope with the same accuracy as for a non-deformed mesh system. To prevent this problem, remeshing is performed at every $\dot{\gamma}t = 0.5$. For the comparison with the prior simulation results [18], a conservative, short-range contact force of the exponential form

$$\boldsymbol{F}_p^{ij} = -F_{ref}\frac{\tau e^{-\tau\epsilon}}{1 - e^{-\tau\epsilon}}\boldsymbol{d} \tag{76}$$

is used. For all dynamic simulations, $\tau = 100$ and $F_{ref}\tau = 6\pi\mu\dot{\gamma}a^2$. Using these parameters, it is observed that the minimum values of ϵ are about 0.001 and 0.0005 at $\phi = 0.3$ and 0.4, respectively. Table 6 shows the simulation parameters used to compute the statistics.

Table 6
Simulation parameters of the dynamic simulations.

ϕ	Ng	N_p	a	Δt
0.3	128^3	4337	0.16	2×10^{-3}
0.4	96^3	1458	0.2532	2×10^{-3}

We define a mean-square residual as

$$\|\boldsymbol{R}\|_M^2 = \frac{1}{N_p}\left(\sum_{i=1}^{6N_p}|r_{f,i}|^2 + \sum_{i=1}^{5N_p}|r_{s,i}|^2\right), \tag{77}$$

in which $\boldsymbol{r}_f$ and $\boldsymbol{r}_s$ are the residuals of $\mathscr{F}^{lub}$ and $\boldsymbol{S}^{tot}$, respectively. The tolerance level δ is chosen as 10^{-3}—10^{-4} to ensure that the error of the particle velocity is $O(10^{-3}$—$10^{-4})$. Using the particle velocities in the previous time step as an initial estimate, the system is solved in under 7—8 iterations. In the concentrated suspensions, due to the complex multi-body hydrodynamic interactions and the elastic contact forces, the trajectories of particles exhibit chaotic motions, which contributes to the random fluctuation of macroscopic variables such as the particle stresses. As a result, a small error in the calculation of the particle velocities is indistinguishable from the statistical noise so that setting very low tolerances does not add to the overall accuracy of a simulation. However, if the tolerance level is set too large, overlap of particles can happen as ϵ is small.

The simulations were performed on a 2.6 GHz AMD Opteron Linux cluster. The computation time for one time step is shown in Fig. 11. All the computations were done using 16 processors and the computation time is the average over $500dt$. It is observed that the computation time is scaled as $\sim N_p$ rather than $\sim N_p logN_p$. This N_p-scaling is the result of the large operation counts in the numerical integration of the force envelope and the projection of the force monopole and dipole to the computational mesh. For example, at $\phi = 0.3$ (Table 6), the number of floating-point operations of the Stokes solver using a Fourier-spectral method is$O(10^7)$ while the numerical integrations to calculate $\boldsymbol{V}$ and $\boldsymbol{E}$ take $O(10^8)$ operations. This integration and projection processes take about 60% of the total computation time while the Stokes solver is about 15%. About 15% of the total computation time is spent on the communications between processors. In the present implementation, MPI collective communications are used in

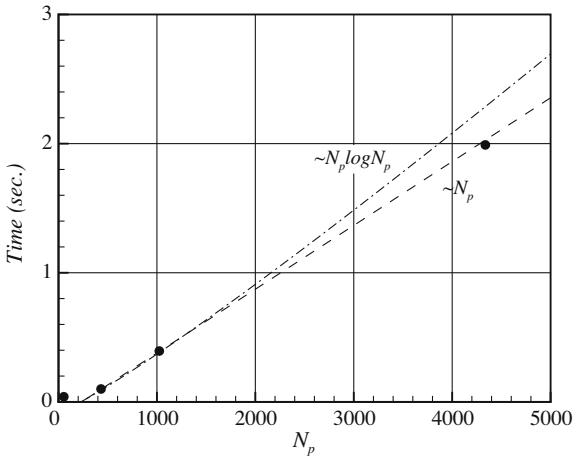

Fig. 11. Computation time of one time step for $\phi = 0.3$.

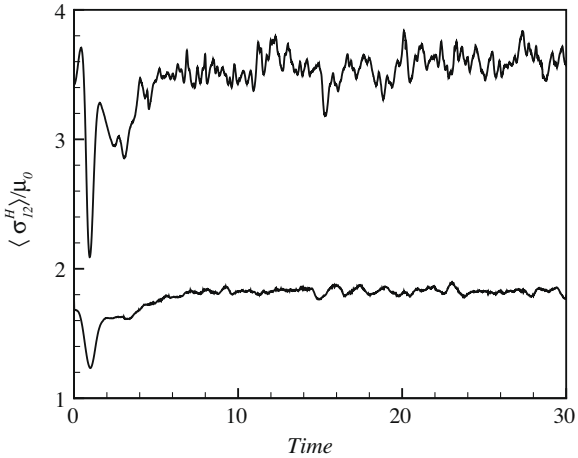

Fig. 12. Time history of the deviatoric stress tensor. The top and bottom curves correspond, respectively, to $\phi = 0.4$ and 0.3.

the FFT and integration–projection processes. By changing the collective communications to the non-blocking communications and overlapping with computations, further speed-up can be achieved.

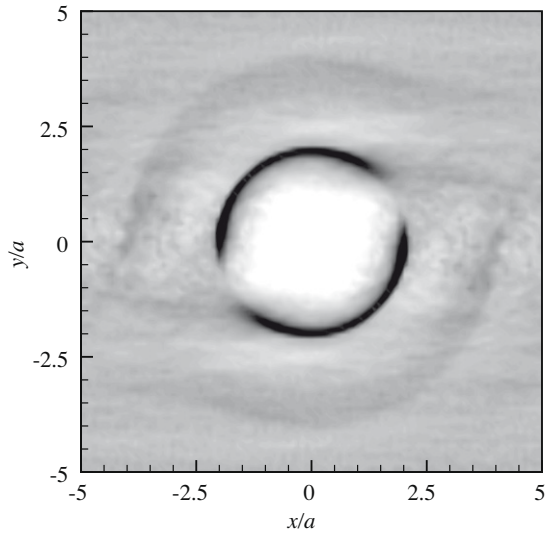

Fig. 13. Projection of the pair-distribution function onto the x–y plane. The darker the contour, the higher the probability is.

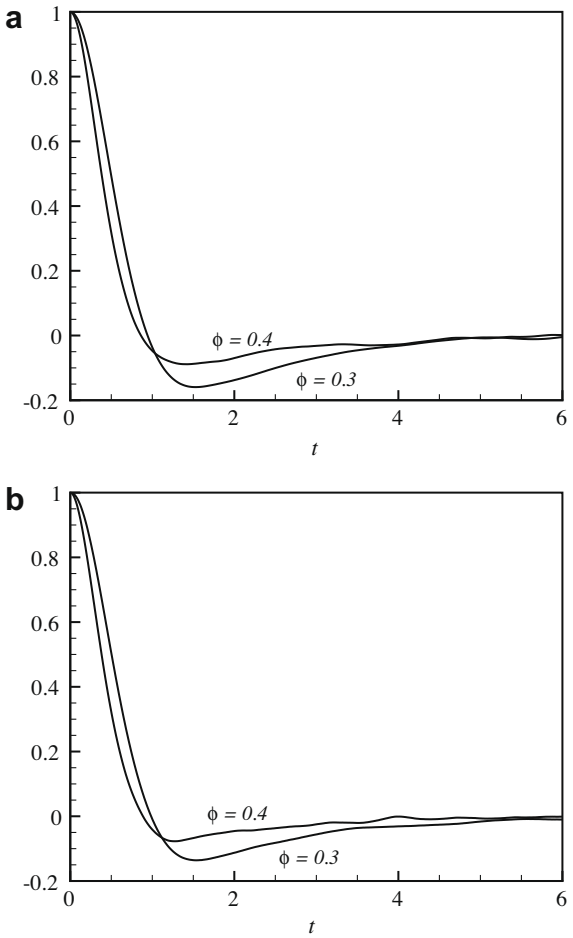

Fig. 14. Velocity auto-correlation functions: (a) $\rho^{V_2}(t)$ and (b) $\rho^{V_3}(t)$ for $\phi = 0.3$ and 0.4.

Fig. 12 shows the time history of the deviatoric stress tensor by hydrodynamic interactions;

$$\langle \boldsymbol{\sigma}^H \rangle = \frac{N_p}{V} \langle \boldsymbol{S} \rangle, \tag{78}$$

in which V is the volume of the sampling domain, in this case the computational domain, and $\langle \cdot \rangle$ denotes ensemble average. Time is normalized by the shear rate, $\dot{\gamma}$. Initial configurations were generated from the body centered cubes with small random perturbations. σ_{12}^H drops sharply at first and starts increasing after $\dot{\gamma}t \simeq 1$ as the microstructure develops in response to the shear flow. To remove the effect of this initial transition, only data for $\dot{\gamma}t > 20$ are used to estimate the statistics.

Fig. 13 shows the pair-distribution function projected onto the $x - y$ plane for $\phi = 0.4$, in which x and y denote the flow and the velocity gradient directions, respectively. In Stokes flow with perfectly smooth hard sphere suspensions, the pair-distribution function should be symmetric due to the reversibility of Stokes equation. However, as shown in Fig. 7, the net displacement caused by the contact force breaks the fore-after symmetry and the probability of finding another particle in the extensive strain direction becomes smaller than the compressible strain direction. The result for the pair-distribution function is consistent with that of Sierou and Brady [42].

A key element for the shear-induced random dispersion of particles in a suspension is the velocity auto-correlation, which is defined as

$$\rho^{V_i}(\tau) = \frac{\langle V_i(t) V_i(t+\tau) \rangle}{\langle V_i(t)^2 \rangle}. \tag{79}$$

Fig. 14 shows the velocity auto-correlation for two volume fractions, $\phi = 0.3$ and 0.4. At the larger volume fraction, the velocity auto-correlation decays faster and the magnitude of the negative peak decreases, which is consistent with the earlier results of [55].

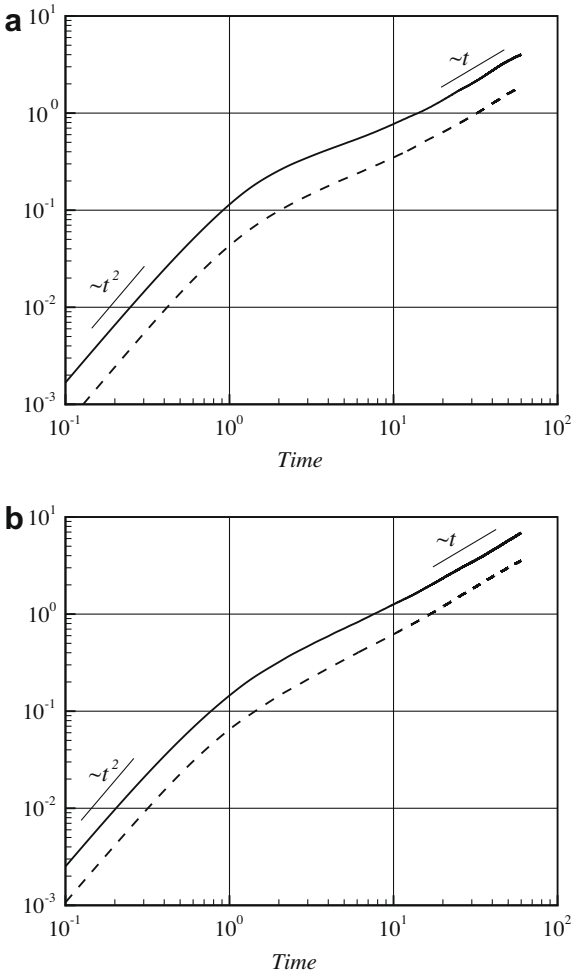

Fig. 15. Mean squared displacement normalized by a^2 in the velocity gradient (solid line) and the vorticity directions (dashed line): (a) $\phi = 0.3$ and (b) $\phi = 0.4$.

Table 7
Diffusion coefficients in y and z directions.

ϕ	D_y	D_z
0.3	0.030	0.016
0.4	0.059	0.037

Fig. 15 shows the mean squared displacement normalized by a^2,

$$\sigma_{Xi}(t) = \frac{\langle (Y_i(t) - Y_i(0))^2 \rangle}{a^2}. \tag{80}$$

It is well known that at short times in which the particle motion is strongly correlated with the initial configuration σ_X increases as $\sim t^2$, while at longer times a steady behavior is established and σ_X shows linear growth with time,

$$\sigma_{Xi}(t) \sim \langle V_i^2 \rangle t^2, \quad t \ll T_{Li}, \tag{81}$$

$$\sigma_{Xi}(t) \sim 2\langle V_i^2 \rangle T_{Li} t, \quad t \gg T_{Li}, \tag{82}$$

in which T_{Li} is the integral timescale in i-direction,

$$T_{Li} = \int_0^\infty \rho^{V_i}(s) ds. \tag{83}$$

The diffusivity D_i is given as

$$D_i = \langle V_i^2 \rangle T_{Li}. \tag{84}$$

The diffusivity can be estimated by two methods. One is from the integral of the velocity auto-correlation function, as shown in Eq. (84) and the other is by estimating the long-term slope of σ_X, which should yield the same results. Table 7 shows the diffusion coefficients evaluated from Eq. (84). The agreement with the previous simulations [18] is quite good.

There is a large scatter in the diffusion coefficients in the literature due to the variation in experimental conditions. In [18], it is found that the diffusion coefficients from SD simulations are almost half of the experimental results. In the experiments, several poorly quantified features, such as surface roughness, surfactant or steric forces, and residual Brownian forces, strongly affect the motion close to contact. In the numerical simulations, the contact force is used to model these effects. Using the contact force (70) with large cut-off distance ($R_{ref} = 2.2$), Abbas et al. [32] could obtain the diffusion coefficients similar to the experimental results. On the other hand, when using the lubrication model by Dance and Maxey [36], the diffusion coefficients were only about 2/3 of those with the large contact forces. Although there are many studies on the role of contact forces on suspensions [19,32,56,55,48], the choice of a contact force to represent the underlying physics correctly is still an open question.

6. Conclusions

In this paper, a new formulation has been derived for the inclusion of lubrication forces between particles in the simulation of viscous suspensions using the force-coupling method. These forces are evaluated on the basis of pairwise additions to the resistance formulation, the inverse of the natural mobility formulation provided by FCM. This provides a more reliable estimate of these effects for concentrated suspensions than using pairwise addition to the mobility problem. Efficient and robust iterative methods are described for solving for the particle stresslets and for lubrication effects in which the problems are written in terms of a symmetric positive definite system. The fully coupled lubrication and far-field interactions are then obtained efficiently through a suitably chosen preconditioned conjugate gradient method, in which the inverse of the ill-conditioned resistance matrix is calculated by a recursive formula. Solving the full system requires typically less than 7–8 iterations while ensuring that the errors in the particle velocity are $O(10^{-3})$ or less.

These methods are tested for the various particle–pair interactions and in concentrated suspensions. For the computation of dynamically evolving, sheared suspensions of neutrally buoyant particles, numerical simulations with $O(1000)$ particles are performed. It is shown that the results are consistent with the previous theories and numerical simulations. It is also shown that the computational cost for homogeneous suspensions in a periodic cell, using a Fourier spectral method, is close to $O(N_p)$. The results also illustrate the importance of near-contact repulsion forces in non-Brownian suspensions and their contribution to the irreversible interaction of particles.

The methods described here may be readily extended to bidisperse or polydisperse systems of particles. For each combination of particles, the corresponding lubrication forces between the particles must be specified as in (44) and as given by [39]. Similarly, the FCM resistance functions for near-field interaction of each combination must be determined as in (45) and a table constructed similar to Table 1. The basic procedures follow as before. The scale coefficient κ in the preconditioner (47) should be adjusted as in Eq. (34).

The force-coupling method can be easily implemented with any existing numerical Stokes or Navier–Stokes solver. As such, the simulation of inhomogeneous and wall-bounded suspensions are possible with FCM. The no-slip boundary condi-

tion at a fixed rigid boundary is then naturally incorporated in the numerical simulation. Lubrication forces must be specified for the interaction of particles with a rigid wall following the same general procedures. There is a minor complication in that the force envelopes (4), (5) are not compact and may extend outside of the flow domain even though the particles are full contained within the domain. The standard procedure has been to truncate the envelopes at the domain boundaries [12]. A more robust implementation, where a simple image particle is introduced, is described by Yeo and Maxey [37]. The implementation for these procedures for Couette flow is also described.

References

[1] A. Popel, P. Johnson, Microcirculation and hemorheology, Annu. Rev. Fluid Mech. 37 (2005) 43.
[2] K. Sharp, R. Adrian, On flow blocking particle structures in microtubes, Microfluid Nanofluid 1 (2005) 376.
[3] H. Wyss, D. Blair, J. Morris, H. Stone, D. Weitz, Mechanism for clogging of microchannels, Phys. Rev. E 74 (2006) 061402.
[4] J.F. Brady, G. Bossis, Stokesian Dynamics, Annu. Rev. Fluids 20 (1988) 111.
[5] B. Cichocki, B.U. Felderhof, Short-time diffusion coefficients and high frequency viscosity of dilute suspensions of spherical Brownian particles, J. Chem. Phys. 89 (1988) 1049.
[6] A.J.C. Ladd, Hydrodynamic transport coefficients of random dispersions of hard spheres, J. Chem. Phys. 93 (1990) 3484.
[7] A.S. Sangani, G. Mo, An $O(N)$ algorithm for Stokes and Laplace interactions of particles, Phys. Fluids 8 (1996) 1990.
[8] C. Pozrikidis, A spectral element method for particulate Stokes flow, J. Comput. Phys. 156 (1999) 360.
[9] N.-Q. Nguyen, A.J.C. Ladd, Lubrication corrections for lattice-Boltzmann simulations of particle suspensions, Phys. Rev. E 66 (2002) 046708.
[10] N.-Q. Nguyen, A.J.C. Ladd, Sedimentation of hard-sphere suspensions at low Reynolds number, J. Fluid Mech. 525 (2005) 73.
[11] M.R. Maxey, B.K. Patel, Localized force representations for particles sedimenting in Stokes flow, Int. J. Multiphase Flow 27 (2001) 1603–1626.
[12] S. Lomholt, M.R. Maxey, Force-coupling method for particulate two-phase flow: Stokes flow, J. Comput. Phys. 184 (2003) 381.
[13] H.H. Hu, D.D. Joseph, M.J. Crochet, Direct simulation of fluid-particle motions, Thoeret. Comput. Fluid Dyn. 3 (1992) 285.
[14] H.H. Hu, Direct simulations of flows of solid–liquid mixtures, Int. J. Multiphase flows 22 (1996) 335.
[15] L. Durlofsky, J.F. Brady, G. Bossis, Dynamic simulation of hydrodynamically interacting particles, J. Fluid Mech. 180 (1987) 21.
[16] B. Cichocki, R.B. Jones, R. Kutteh, E. Wajnryb, Friction and mobility for colloidal spheres in Stokes flow near a boundary: the multipole method and applications, J. Chem. Phys. 112 (2000) 2548.
[17] A. Sierou, J.F. Brady, Accelerated Stokesian Dynamics simulations, J. Fluid Mech. 448 (2001) 115.
[18] A. Sierou, J.F. Brady, Shear-induced self-diffusion in non-colloidal suspensions, J. Fluid Mech. 506 (2004) 285.
[19] M.S. Ingber, S. Feng, A.L. Graham, H. Brenner, The analysis of self-diffusion and migration of rough spheres in nonlinear shear flow using a traction-corrected boundary element method, J. Fluid Mech. 598 (2008) 267.
[20] C. Pozrikidis, Dynamical simulation of the flow of suspensions: wall-bounded and pressure-driven channel flow, Ind. Eng. Chem. Res. 41 (2002) 6312.
[21] C. Pozrikidis, Flipping of an adherent blood platelet over a substrate, J. Fluid Mech. 568 (2006) 161.
[22] R. Verberg, D.L. Koch, Rheology of particle suspensions with low to moderate fluid inertia at finite particle inertia, Phys. Fluids 18 (2006) 083303.
[23] P.M. Kulkarni, J.F. Morris, Pair-sphere trajectories in finite-Reynolds-number shear flow, J. Fluid Mech. 596 (2008) 413.
[24] J.R. Blake, A.T. Chwang, Fundamental singularities of viscous flow, J. Eng. Math. 8 (1974) 23.
[25] J.W. Swan, J.F. Brady, Simulation of hydrodynamically interacting particles near a no-slip boundary, Phys. Fluids 19 (2007) 113306.
[26] P.R. Nott, J.F. Brady, Pressure-driven flow of suspensions: simulation and theory, J. Fluid Mech. 275 (1994) 157.
[27] A. Singh, P.R. Nott, Normal stresses and microstructure in bounded sheared suspensions via Stokesian Dynamics simulations, J. Fluid Mech. 412 (2000) 279.
[28] P.G. Saffman, On the settling speed of free and fixed suspensions, Stud. Appl. Math. LII (1973) 115.
[29] S. Lomholt, B. Stenum, M.R. Maxey, Experimental verification of the force coupling method for particulate flows, Int. J. Multiphase flow 28 (2002) 225.
[30] S.L. Dance, E. Climent, M.R. Maxey, Collision barrier effects on the bulk flow in a random suspension, Phys. Fluids 16 (2004) 828.
[31] S.L. Dance, M.R. Maxey, Particle density stratification in transient sedimentation, Phys. Rev. E 68 (2003) 031403.
[32] M. Abbas, E. Climent, O. Simonin, M.R. Maxey, Dynamics of bidisperse suspensions under Stokes flows: linear shear flow and sedimentation, Phys. Fluids 18 (2006) 121504.
[33] J. Xu, M.R. Maxey, G.E. Karniadakis, Numerical simulation of turbulent drag reduction using micro-bubbles, J. Fluid Mech. 468 (2002) 271.
[34] E.E. Keaveny, M.R. Maxey, Interaction between comoving magnetic microswimmers, Phys. Rev. E 77 (2008) 041910.
[35] D. Liu, E.E. Keaveny, M.R. Maxey, G.E. Karniadakis, Force coupling method for flows with ellipsoidal particles, J. Comput. Phys. 228 (2009) 3559.
[36] S.L. Dance, M.R. Maxey, Incorporation of lubrication effects into force-coupling method for particulate two-phase flow, J. Comput. Phys. 189 (2003) 212.
[37] K. Yeo, M.R. Maxey, Dynamics of concentrated suspensions of non-colloidal particles in Couette flow, J. Fluid Mech., 2010, in press.
[38] H. Brenner, M.E. O'Neill, On the Stokes resistance of multiparticle systems in a linear shear field, Chem. Eng. Sci. 27 (1972) 1421.
[39] S. Kim, S.J. Karrila, Microhydrodynamics: Principles and Selected Applications, Butterworth-Heinemann, 1991.
[40] E. Climent, Personal communication.
[41] J.J. Dongarra, I.S. Duff, D.C. Sorensen, H.A. van der Vorst, Numerical Linear Algebra on High-Performance Computers, SIAM, 1998.
[42] A. Sierou, J.F. Brady, Rheology and microstructure in concentrated noncolloidal suspensions, J. Rheol. 46 (2002) 1031.
[43] D.J. Jeffrey, Y. Onishi, Calculation of the resistance and mobility functions for two unequal rigid spheres in low-Reynolds-number flow, J. Fluid Mech. 139 (1984) 261.
[44] K. Ichiki, Improvement of the Stokesian Dynamics method for systems with a finite number of particles, J. Fluid Mech. 452 (2002) 231.
[45] P. Ganatos, R. Pfeffer, S. Weinbaum, A numerical-solution technique for three-dimensional Stokes flows, with application to the motion of strongly interacting spheres in a plane, J. Fluid Mech. 84 (1978) 79.
[46] G.K. Batchelor, J.T. Green, The hydrodynamic interaction of two small freely-moving spheres in a linear flow field, J. Fluid Mech. 56 (1972) 375.
[47] G.K. Batchelor, J.T. Green, The determination of the bulk stress in a suspension of spherical particles to order c^2, J. Fluid Mech. 56 (1972) 401.
[48] F.R. Da Cunha, E.J. Hinch, Shear-induced dispersion in a dilute suspension of rough spheres, J. Fluid Mech. 309 (1996) 211.
[49] J.R. Smart, D.T. Leighton, Measurement of the hydrodynamic surface roughness of noncolloidal spheres, Phys. Fluids A 1 (1989) 52.
[50] K.C. Nunan, J.B. Keller, Effective viscosity of a periodic suspension, J. Fluid Mech. 142 (1984) 269.
[51] J.M.A. Hoffman, Ph.D. Thesis, Technische University, Eindhoven, 1999.
[52] I.M. Krieger, T.J. Dogherty, A mechanism for non-newtonian flow in suspensions of rigid spheres, Trans. Soc. Rheol. 3 (1959) 137.
[53] J.J. Stickel, R.L. Powell, Fluid mechanics and rheology of dense suspensions, Ann. Rev. Fluid Mech. 37 (2005) 129.
[54] R.S. Rogallo, Technical Report 81315, NASA, 1981.
[55] G. Drazer, J. Koplik, B. Khusid, A. Acrivos, Deterministic and stochastic behavior of non-Brownian spheres in sheared suspensions, J. Fluid Mech. 460 (2002) 307.
[56] A. Meunier, G. Bossis, The influence of surface forces on shear-induced tracer diffusion in mono and bidisperse suspensions, Eur. Phys. J. E 506 (2004) 285.